Appendix 1 – Environmental Models

A1.1 Gravity Model

The gravitational attraction of the Earth is by far the strongest influence in near-Earth space, and approximates a spherical field. In this simplification, the attractive force vector between the Earth and a body in near-Earth space has a magnitude of...

$$F = \frac{GMm}{r^2}$$

...in which G is the universal gravitational constant, M is the mass of the Earth, m is the mass of the body and r is the distance between the body and the centre of the Earth.

A1.1.1 Spherical Harmonic Effects

A1.1.1.1 Zonal Harmonics

This simple model ignores the fact that the Earth is not a uniform sphere. In reality, the shape of the Earth approximates more closely an oblate spheroid with an oblateness of 1 part in 298.257. This oblateness arises because the Earth is rotating about its polar axis, generating a centrifugal force which increases with co-latitude.

The equatorial bulge of the Earth tends to strengthen the gravitational attraction at a given geocentric altitude above the equator. This phenomenon is known as the J_2 effect, after Sir Harold Jeffreys.

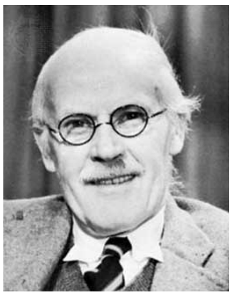

Figure A1-1 Sir Harold Jeffreys

J_2 is, however, just the strongest term in a series of zonal harmonics which describe the variation of the magnitude of the gravitational force vector in near-Earth space. The complete expansion of the magnitude of the force vector at a given latitude ϕ with respect to these harmonics is estimated as follows, after the geopotential equation set out by mit.edu (2007).

$$F = -\nabla \frac{GMm}{r} \left\{ 1 - \sum_{n=2}^{\infty} J_n \left(\frac{R}{r} \right)^n P_n(\sin \phi) \right\}$$

The value of the J_n terms in the expansion must be determined by examination of the orbits of low-drag spacecraft. The first few terms are...

J_2	1082626 x 10^{-9}
J_3	-2530 x 10^{-9}
J_4	-1624 x 10^{-9}
J_5	-245 x 10^{-9}
J_6	543 x 10^{-9}

The P_n terms in the expansion are the Legendre polynomials, the first few terms (P_0 and P_1 neglected) and general form of which are as follows...

$$P_2(x) = \frac{1}{2}\left(3x^2 - 1\right)$$

$$P_3(x) = \frac{1}{2}\left(5x^3 - 3x\right)$$

...

$$P_n(x) = \left(\frac{1}{2^n n!}\right)\left(\frac{d^n}{dx^n}\right)\left(x^2 - 1\right)^n$$

Each term describes a different variation in the gravity field. For example, the J_2 effect describes the equatorial bulge, J_3 describes a tendency towards a three-petalled profile, J_4 towards a four-petalled profile, and so on.

A1.1.1.2 Sectoral and Tesseral Harmonics

As well as zonal harmonics, which produce bands of constant deviation from the spherical field along lines of latitude, there are sectoral and tesseral harmonics. These harmonics produce a similar effect with varying longitude, which is denoted by λ. To calculate their effect, the harmonic approximation must be expanded further to accommodate some new terms.

$$F = -\nabla \frac{GMm}{r}\left\{1 - \sum_{n=2}^{\infty} J_n \left(\frac{R}{r}\right)^n P_n(\sin\phi) + \sum_{l=2}^{\infty}\sum_{m=1}^{l}\left(\frac{R}{r}\right)^l P_{l,m}(\sin\phi)\left(\overline{C}_{l,m}\cos m\lambda + \overline{S}_{l,m}\sin m\lambda\right)N_{l,m}\right\}$$

The normalised constants $\overline{C}_{l,m}$ and $\overline{S}_{l,m}$ (in which $m \leq l$) are analogous to the J_n terms, and have been calculated in the same way. The first few are as follows...

l	m	$\overline{C}$	$\overline{S}$
2	1	-1 x 10^{-9}	-3 x 10^{-9}
2	2	2438 x 10^{-9}	-1399 x 10^{-9}
3	1	2029 x 10^{-9}	250 x 10^{-9}
3	2	904 x 10^{-9}	-616 x 10^{-9}
3	3	723 x 10^{-9}	1415 x 10^{-9}

The Legendre expansion itself must also be expanded more fully to provide terms of degree l and order m, again with $m \leq l$. The first few terms and the general form are as follows...

$$P_{2,1}(x) = 3x\left(1 - x^2\right)^{\frac{1}{2}}$$

$$P_{2,2}(x) = 3x\left(1 - x^2\right)$$

...

$$P_{l,m}(x) = \left(\frac{\left(1 - x^2\right)^{\frac{m}{2}}}{2^l\, l!}\right)\left(\frac{d^{\,l+m}}{dx^{l+m}}\right)\left(x^2 - 1\right)^l$$

Finally, the normalising factor $N_{l,m}$ can be given as follows...

$$N_{l,m} = \left\{\frac{2(l - m)!(2l + 1)}{(l + m)!}\right\}^{\frac{1}{2}}$$

Incidentally, a harmonic is known as a sectoral harmonic when $l = m$, and as a tesseral harmonic when $l \neq m$.

A1.1.1.3 The Sum of the Zonal, Sectoral and Tesseral Harmonics

The effect of zonal, sectoral and tesseral harmonics on the magnitude of the gravitational force vector may be illustrated by considering their effect on the shape of the geoid. The geoid is simply a three dimensional shape, the surface of which has a constant gravitational potential. If there were no tides, currents or winds, sea level across the globe would conform to the geoid.

Figure A1-2 below illustrates the different effects of the harmonics. Zonal harmonics produce variation with latitude, sectoral harmonics produce variation with longitude and tesseral harmonics produce variation in both.

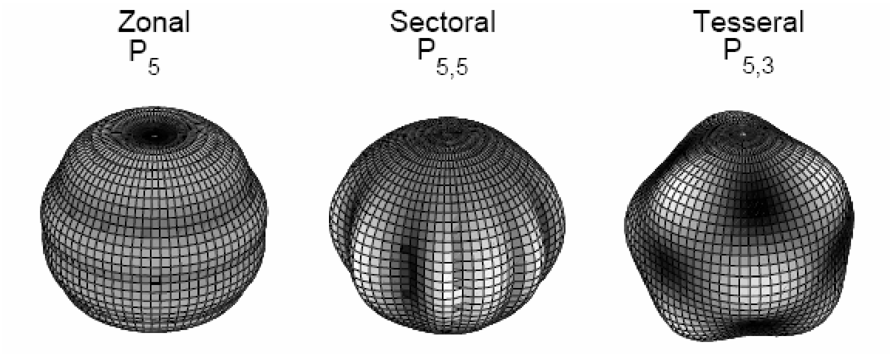

Figure A1-2 Zonal, sectoral and tesseral spherical harmonics

The WGS-84 gravity model has harmonics to degree and order 180, but in practice a good gravity model, such as the Goddard Earth Model 10B described by Lerch (1981), will go to degree and order 36 and describe the surface of the geoid to an accuracy of 1 m.

An approximation of the surface of the geoid is found in Figure A1-3.

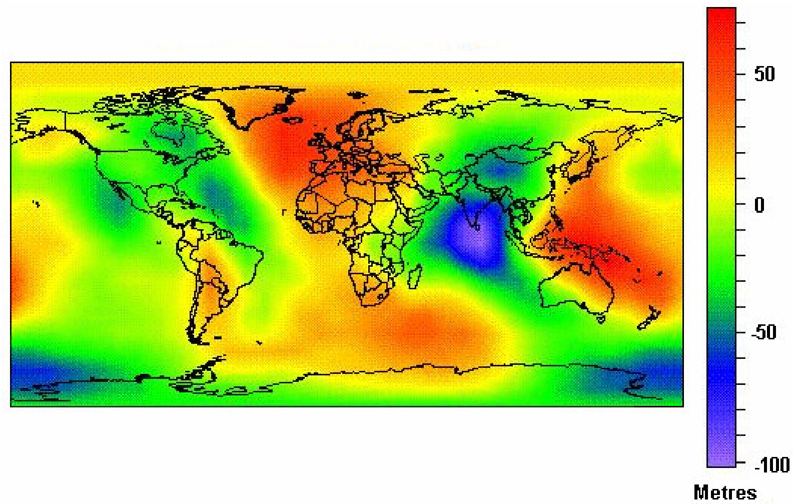

Figure A1-3 The geoid, adapted from fredonia.edu (2006)

The red area in the north Atlantic illustrates a region where the geoid rises to about 65 m above a perfect oblate spheroid with oblateness equal to 1 part in 298.257. The purple area south of India represents a dip to 104 m below the perfect spheroid. This implies strong gravity over the north Atlantic and weak gravity south of India.

A1.1.2 Non Spherical Harmonic Effects

Until recently, it had been observed that the geoid was becoming progressively more spherical, in particular due to a gradual reduction in the strength of the J_2 harmonic. This was, and still is, thought to be due to the ongoing upward motion (or *isostatic rebound*) of the north polar region, which until the end of the Pleistocene (approximately 15,000 years ago) had been pressed downwards by the weight of vast ice sheets. The south polar region was less affected because the Southern Ocean prevented the ice sheets from spreading beyond the Antarctic continent.

However, it has been observed by Cox (2002) that this process reversed in 1998 and the Earth has been growing more oblate ever since. The causes of this phenomenon are not fully understood at present, although a redistribution of the oceans due to changing current patterns may be to blame. In particular, increased melt rates of the northern ice cap may be strengthening fresh south-bound currents such as the Labrador and West Greenland current.

A1.1.3 The Simulation Model

The MathWorks provide a model (WGS-84) in their Aerospace Blockset which goes to degree and order 180, but licensing is very expensive and the extra calculation involved is appreciable. During the simulations of the deorbit device one copy of this model was used as a control, but the vast majority were carried out using a much simplified model which evaluates the J_2 term only.

The J_2 term is perhaps 500 times stronger than the next strongest harmonic and is also stronger than the lunisolar perturbations up to the altitude of GEO. It is therefore reasonable to assume that the perturbations caused by these factors will be negligible in LEO. This assumption is borne out by the similar behaviour found in response to the control WGS 84 model and the simplified J_2-only model.

To simplify the determination of a usable force vector, the grad operator is removed and the following approximation used. This approximation will give a good approximation of the vertical component of force at the expense of neglecting the horizontal component.

$$F = \frac{GMm}{r^2}\left\{1 - \sum_{n=2}^{\infty} J_n \left(\frac{R}{r}\right)^n P_n(\sin\phi)\right\}$$

A1.2 Atmosphere Model

The aerodynamic load experienced by any device moving through the upper atmosphere will be proportional to the density of the rarefied gas found there, but according to King-Hele (1987) this density is notoriously difficult to predict. Density variation exhibits some regularity in response to generally predictable factors such as altitude, solar activity, time of year, time of day and the local latitude; but also occurs in response to largely unpredictable factors such as the geomagnetic index and the presence and strength of any El Niño effect.

A1.2.1 Factors affecting Atmospheric Density

A1.2.1.1 Behaviour in response to Altitude

According to King-Hele (1987), altitude is the single most important factor influencing the density of the atmosphere. Density falls from an almost constant value of 1.225 kg/m^3 at sea level (with perhaps 2% variation in deep Atlantic depressions) to 1 g/km^3 at between 400 km and 600 km, depending on the state of the factors described above.

As one ascends through the lower atmosphere, turbulence thoroughly mixes all the different gas species and ensures homogeneity. However, at 90 km to 100 km turbulence begins to weaken, fading out completely at an altitude known as the turbopause. Above this level the constituent gases tend to separate into fractions according to their molecular weights.

This stratified structure tends to interrupt the expected continuous exponential reduction in density and separates it into a series of different exponential decay zones, each fading seamlessly into the next. As would be expected, the denser species such as nitrogen and atomic oxygen predominate at lower altitudes (up to approximately 170 km and 500 km respectively), with helium and hydrogen becoming increasingly important at higher altitudes.

A1.2.1.2 Behaviour in response to Solar Activity

The sun exhibits an eleven-year activity cycle, characterised by a rapid rise in activity for approximately four years, followed by a more gradual decline. The activity is primarily defined by the $F_{10.7}$ index which may, over the course of a typical cycle, progress from 80 x 10^4 Jy up to 220 x 10^4 Jy, followed by a slow reduction back to the original level.

The eleven-year solar cycle has been recorded since the 1600s because it is closely tied to the number and latitude of the easily-observable sunspot population. As a result of this long recorded history, the solar cycle which peaked in 2000 – 2001 was designated cycle # 23 and detailed predictions for the $F_{10.7}$ index over the course of that cycle were made beforehand by NASA (1996).

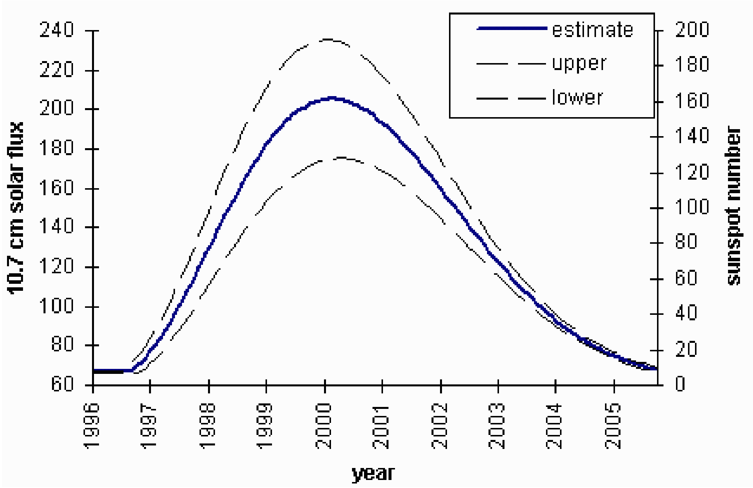

Figure A1-4 Solar activity prediction for Cycle 23 (reproduced from NASA (1996))

High solar activity is associated with large numbers of high-energy photons. These photons heat the atmosphere, causing the lower strata to expand upwards and increase the ambient density in LEO.

In previous years, high values of the $F_{10.7}$ index have been associated with 3-, 8- and 20-fold increases in atmospheric density at 250 km, 400 km and 600 km respectively.

A1.2.1.3 Behaviour in response to Time of Year

In a typical year, after the effects of solar activity have been removed, the atmospheric density shows maxima in April and late October and minima in January and July. The second annual maximum and minimum tend to be stronger than the first, and the strength of the effect as a whole is inversely proportional to the solar activity level.

A1.2.1.4 Behaviour in response to Time of Day

As the sun rises over any region of the Earth's atmosphere, it heats the gases and causes thermal expansion. As before, this causes the lower layers of the atmosphere to expand upwards, increasing the density at higher altitudes.

The peak density at any altitude above approximately 200 km tends to occur at around 1400 h, whilst the minimum density occurs at around 0400 h. The daytime peak is better defined than the night-time trough, as illustrated in Figure A1-5, which has been adapted from King-Hele (1987).

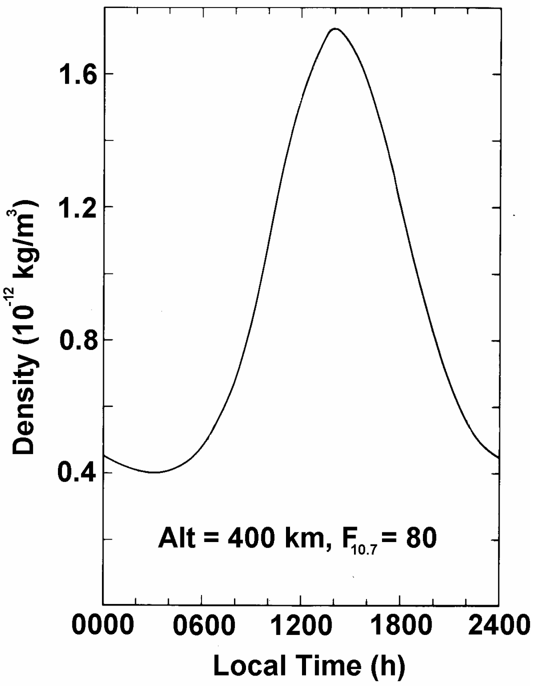

Figure A1-5 Daily variation in atmospheric density in an equatorial orbit, adapted from King-Hele (1987)

A1.2.1.5 Behaviour in response to Latitude

The density of the upper atmosphere at a given point in time is a function of latitude, not due to any inherent effect of latitude itself but rather due to the effect of the seasons.

It has already been stated that the atmosphere becomes denser at altitude due to the thermal expansion of the lower layers, an effect which is naturally more pronounced during the summer months. Increased density may therefore be expected over the summer hemisphere.

A1.2.1.6 Behaviour in response to Geomagnetic Planetary Index

The geomagnetic planetary index (a_p) is a measure of the disturbance in the Earth's magnetic field caused by transient events such as solar flares and coronal mass ejections. Although the average value of this index exhibits a very weak correlation with the $F_{10.7}$ index over the eleven year cycle, its main variation is on an hour-to-hour basis, over which fluctuations 10 times greater than the cyclical variation may occur.

Disturbances in the Earth's magnetic field induce electrical currents in the atmosphere, which heat it and increase the density at high altitudes. The largest of these events may boost density by a factor of 8 at 600 km, but the effect is always transient and fades away within a few hours, probably not to be repeated for several weeks or months.

A1.2.2 Summary of Atmospheric Density

The density of the upper atmosphere may be expected to decrease as one ascends, but the rate of decrease will be reduced at periods of high solar activity. In addition, density will be increased where local heating occurs due to the thermal expansion of the lower layers. Finally, density will be higher than average in spring and autumn, and lower in winter and summer.

These effects are deeply intertwined. For example, according to King-Hele (1987) the diurnal variation may cause the peak density during the day to be 1.1 times the average value at 200 km, 1.5 times the average at 400 km, 1.7 times the average at 600 km and 1.5 times the average at 800 km. However, those values only apply at times of low solar activity – at other times factors of 1.1, 1.3, 1.5 and 1.6 would be more accurate. The annual variation must also be taken into account, remembering that the strength of this variation is dependant on the solar activity as well. Finally, fluctuations caused by transient solar events can swamp all of the above effects, albeit only for a few hours.

A1.2.3 The Simulation Model

The simulation model which attempts to predict this behaviour is based upon the MSIS-90 mode (NASA (2005)), which is in turn a revised version of the MSIS-86 model described by Hedin (1987). The MSIS, or Mass Spectrometer Incoherent Scatter, models are based on observations of the motion of spacecraft and the measurements of several incoherent scatter radars.

The MSIS-90 model seeks to calculate the effects of each individual gas species and then sum the result to obtain the total density, as well as other parameters such as pressure and temperature. Although the results agree well with observations, there has been some disagreement with regard to the densities of individual species, such as the discussion of the densities of He and O^+ given by Uy (1997).

A1.2.3.1 The MSIS-90 Look-Up Table

The MSIS-90 model code is a very long file, and is only available in FORTRAN. To include the MSIS model in a simulation of the performance of the deorbit device in its current form would therefore result in very slow simulations because the long FORTRAN file would have to be called at each timestep. To avoid this problem, the FORTRAN file has been pre-run for 75,600 key conditions, distributed according to the following breakpoints.

Solar Activity	$F_{10.7}$ = 100 x 10^4 Jy, 150 x 10^4 Jy and 200 x 10^4 Jy.
Time of Year	Date = 1st Jan, 1st Mar, 1st May, 1st Jul, 1st Sep, 1st Nov.
Time of Day	Time = 0000 h, 0400 h, 0800 h, 1200 h, 1600 h, 2000 h.
Latitude	Lat = 90°S, 60°S, 30°S, 0°, 30°N, 60°N 90°N.
Altitude	Alt = 200 km – 700 km, in 5 km steps.

The variation of the a_p index was neglected due to its high degree of unpredictability, and a value of 15 was used throughout.

The densities predicted can then be written to a five-dimensional Simulink Look-Up Table. This Look-Up Table contains 75,600 unique data points, which increases to 102,900 when the data is expanded to cover complete daily and annual cycles. Each data point represents the density predicted by the MSIS-90 model for a particular combination of altitude, hour-angle, latitude, month and solar activity.

The data within the Look-Up Table is presented in a much-reduced form in Figure A1-6. The three columns represent data for low, medium and high levels of solar activity ($F_{10.7}$ = 100 x 10^4 Jy, 150 x 10^4 Jy and 200 x 10^4 Jy), whilst the six rows refer to the time of year (1^{st} January, 1^{st} March, 1^{st} May *etc.*).

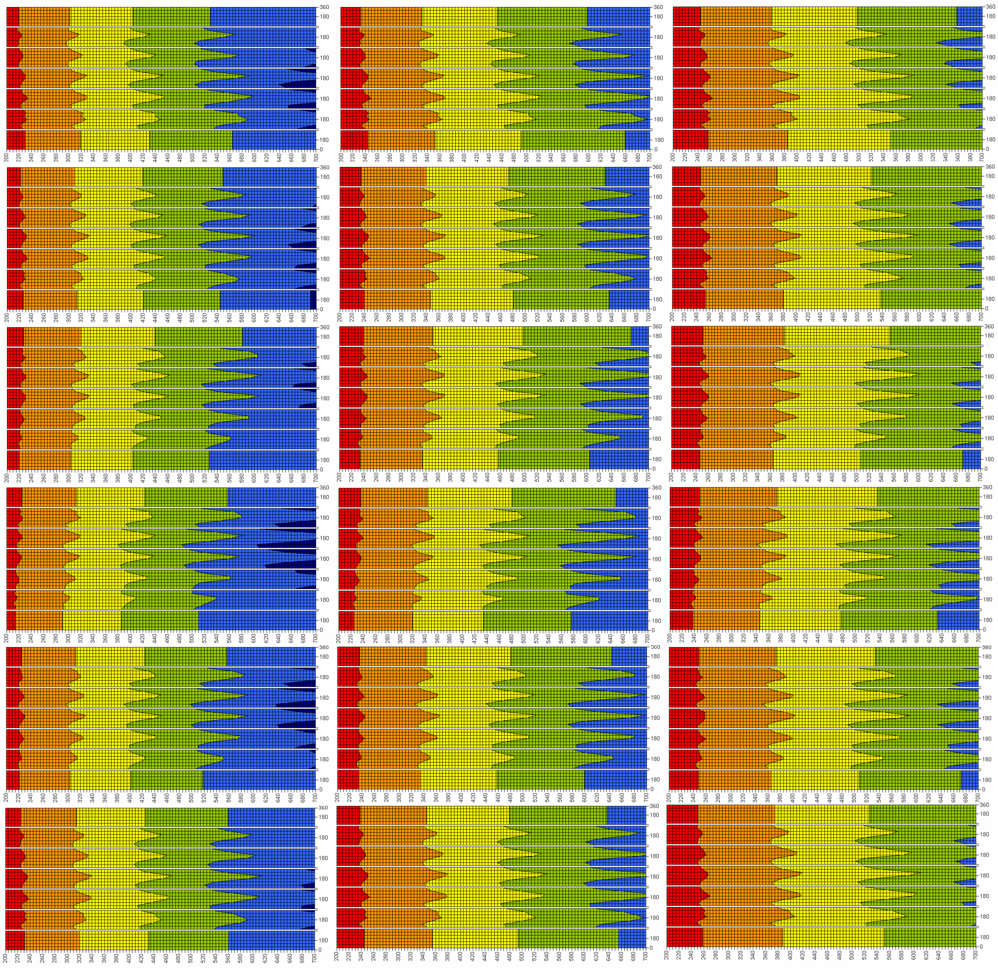

Figure A1-6 Simplified contents of the MSIS-90 Look-Up Table

To examine the effect of latitude, time of day and altitude, Figure A1-7 focuses on the data for the 1^{st} of May at a time of medium solar activity.

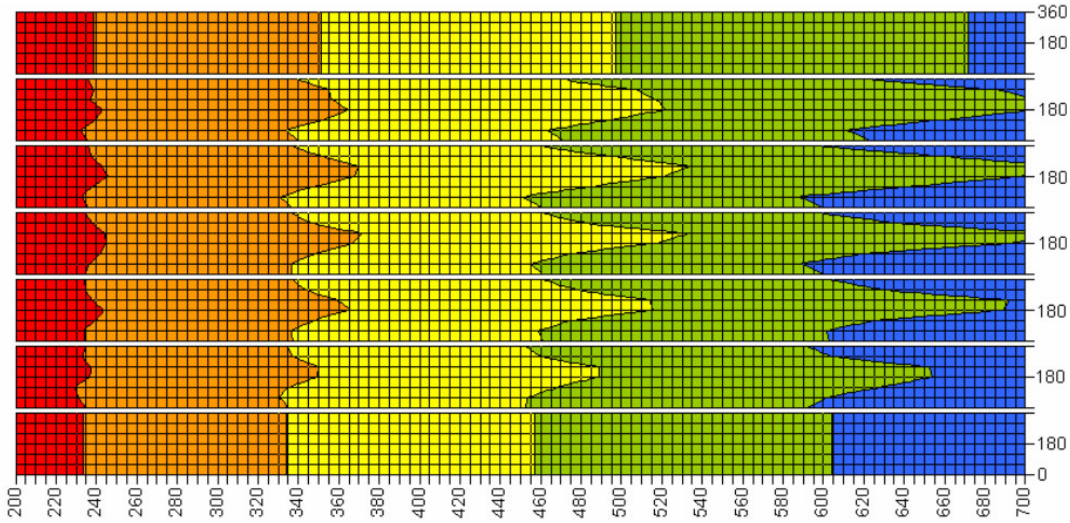

Figure A1-7 Part of the simplified contents of the MSIS-90 Look-Up Table

Each of the seven bars contains data for a specific latitude, starting at 90°N at the top and progressing to 90°S at the bottom. Each bar is then a representation of the predicted density throughout the course of a day, from local midnight at the bottom to local midnight at the top. The altitude increases left-to-right from 200 km to 700 km.

Each band of colour represents a 10-fold variation in density, from the order of 1 x 10^{-10} kg/m^3 in the red zone to the order of 1 x 10^{-15} kg/m^3 in the purple zone.

A1.3 Magnetic Model

The extra damping requirement of the deorbit device, over and above that which can be generated by aerodynamic forces, is met by means of interaction with the Earth's magnetic field.

The flux density induced by a magnetic field may be given by...

$$B = \mu_0 \mu_{rel} H$$

...in which B is the flux density in Tesla; μ_0 is the permeability of free space (1.257 x 10^{-6} Farads per metre); μ_{rel} is the relative permeability of the body, which is simply a multiplier on μ_0; and H is the magnetic field strength in amps per metre.

A1.3.1 Spherical Harmonic Effects

Like the gravity field, the magnetic field can be described by spherical harmonics. The coefficients known as l and m in the gravitational expansion are known in geomagnetic circles as Gauss coefficients after Carl Gauss, who evaluated them to the fourth order and degree in 1838.

Figure A1-8 Carl Gauss

A1.3.1.1 Intensity, Declination and Inclination

The evaluation of the expansion of the Gauss coefficients reveals the strength and direction of the magnetic field, which is usually defined by intensity, declination and inclination. Intensity is the flux density measured in nT, whilst declination and inclination are the angles by which the geomagnetic north-seeking flux lines deviate from local true north and local horizontal respectively. Positive declination indicates a variance to the east, whilst positive inclination indicates the flux is dipping below the horizontal.

A1.3.1.1.1 Intensity

The total sea-level flux density, in nT, predicted by the 2005 US/UK World Magnetic Model is shown in Figure A1-9. The maximum values near the magnetic poles are in the region of 60,000 nT, whilst the minimum values found in the South Atlantic anomaly are below 25,000 nT. By way of comparison, a typical fridge magnet produces a flux density of about 5 mT, or around 100 times the background field.

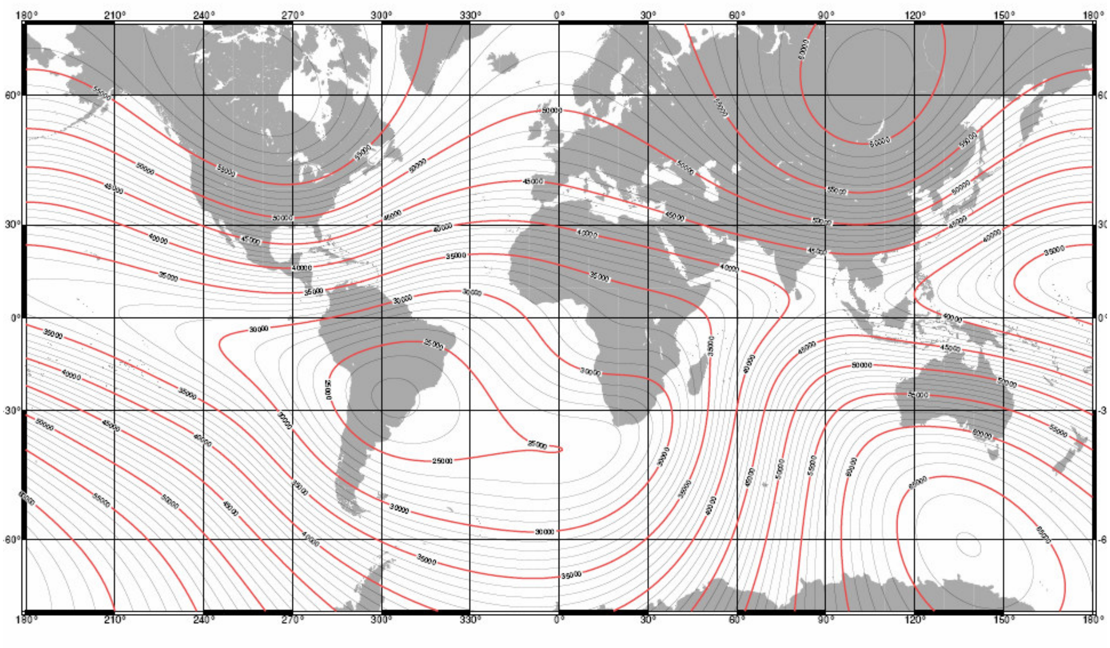

Figure A1-9 – Magnetic Flux Density

The flux density decreases with altitude to about 100 nT at geostationary altitude, but at this level it is heavily and dynamically influenced by the sun's more powerful field. In the LEO regime the field is reasonably stable, but the intensity at 600 km falls by a factor of approximately two compared to the sea-level intensity.

A1.3.1.1.2 Declination

The sea-level declination angle predicted by the 2000 US/UK World Magnetic Model is as shown in Figure A-10.

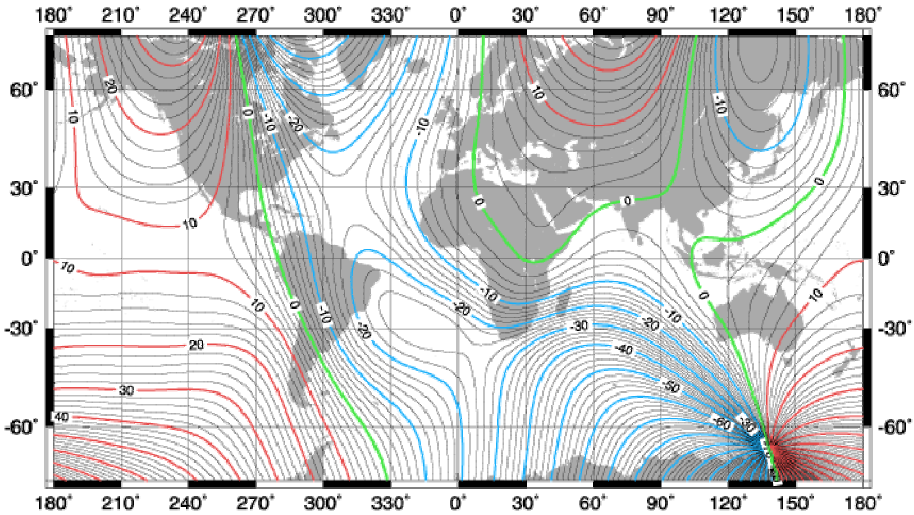

Figure A1-10 – Magnetic Declination Angle

A1.3.1.1.3 Inclination

The sea-level inclination angle predicted by the 2000 US/UK World Magnetic Model is as shown in Figure A-11.

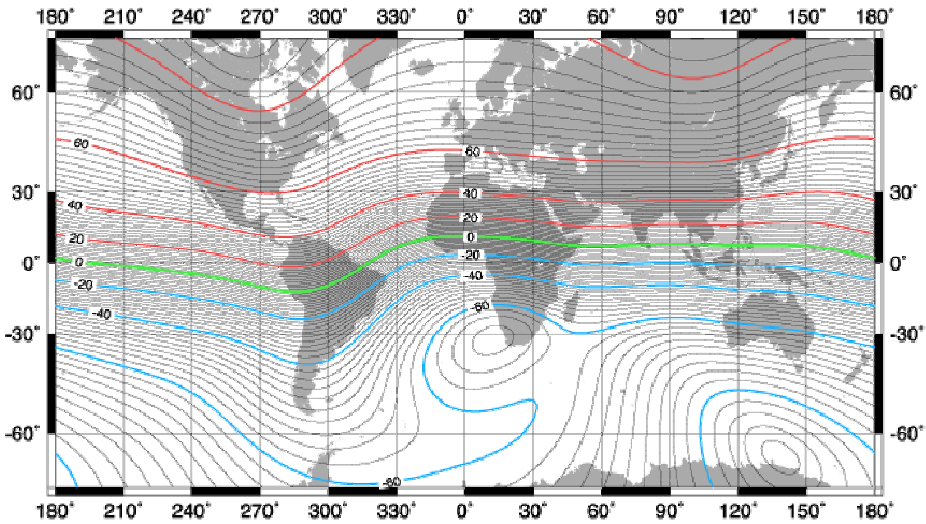

Figure A1-11 – Magnetic Inclination Angle

A1.3.2 Non Spherical Harmonic Effects

A1.3.2.1 Geological Variation

The Earth's magnetic field has varied greatly throughout geological time, with the field (and magnetic poles) reversing completely every 300,000 years or so. Each reversal takes about 10,000 years to complete, during which time the field intensity drops to around 10% of its normal strength. As a reversal approaches the field may exhibit increasing numbers of excursions, where the field strength briefly weakens and the magnetic poles wander erratically towards the equator before normality is restored.

The current period of 'normal' polarity, which has persisted for 730,000 years, is termed the Brunhes normal chron. This extended duration, although above average, is by no means exceptional. In the Cretaceous period a normal chron (the Cretaceous normal superchron) persisted for 35 million years, and in the Permian period a reversed chron (the Kiaman reversed superchron) persisted for some 50 million years.

These variations have been of great importance in geological research, but take place over much too long a timescale to have any influence on the performance of the deorbit device.

A1.3.2.2 Short Term (secular) Variation

Over the course of the past few hundred years, the declination of the field at London has varied between 11° E and 25° W, whilst the field intensity has fallen by around 5 % per century. This corresponds to the magnetic field moving at a rate of approximately 1 metre per hour relative to the geographic surface.

On a timescale of years, the field may experience jerks in the secular variation, where the rate of change rises for a few months before returning to normal. Some recent jerks occurred in 1925, 1969 and 1978.

These secular variations, even during a jerk period, take place over much too long a timescale to have any influence on the performance of the deorbit device.

A1.3.3 The Simulation Model

The simulation model is based on the 2005 IGRF models available from NOAA (2006), which calculate the magnetic field parameters using an expansion of degree and order 10.

A1.3.3.1 The IGRF Look-Up Table

A Look-Up Table similar to that used for the atmospheric density information was constructed to hold the data on the strength, declination and inclination of the magnetic field generated by the IGRF model. Part of the data (the sea level field strength only) within the Look-Up Table is presented in a much-reduced form in Figure A1-12.

Because the magnetic field is not as volatile as the atmosphere, does not vary as much with altitude, and leads to smaller torques than the aerodynamic effects the Look-Up Table used to codify it the magnetic field can be proportionally coarser.

The IGRF Look-Up table therefore only evaluates the field at every 30° of latitude and 60° of longitude for altitudes of 200 km, 400 km and 600 km; thus incorporating 105 data points of which just 90 are unique.

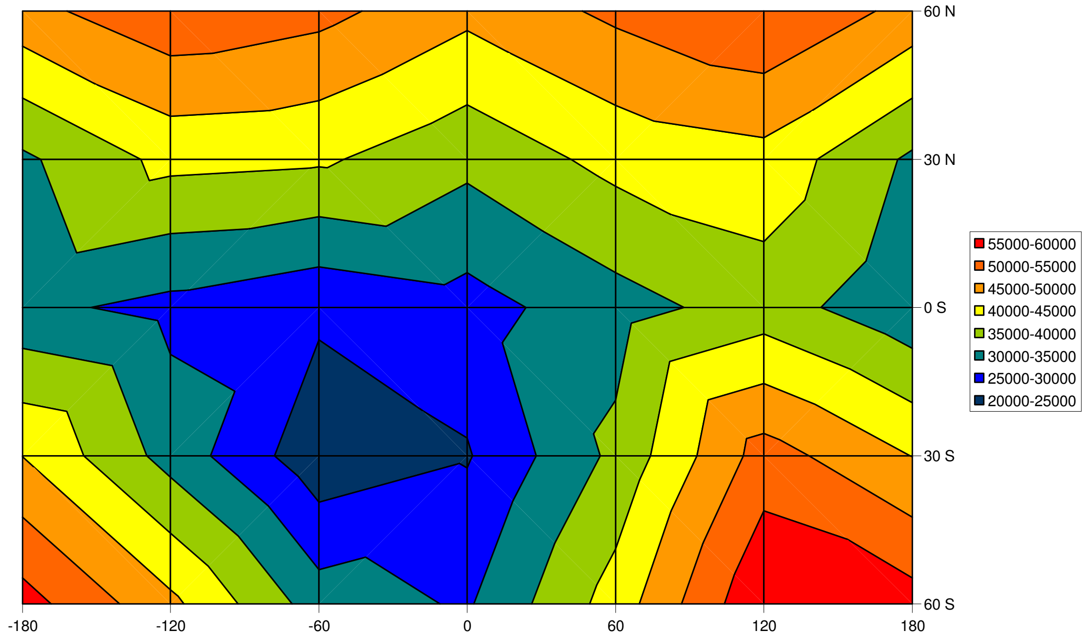

Figure A1-12 Simplified, reduced contents of the IRGF Look-Up Table. Compare with the data presented in Figure A1-9.

Appendix 2 – Matlab m-files

A2.1 *Boom.m*

```
% BOOM - A program to calculate the required skin thickness and
% resultant mass of an inflated boom of given radius able to
% withstand a given Bending Moment.
%
% Call Syntax:
% Boom(Moment,r,YS,Design_Efficiency,SG,R,Temp_Shadow,Temp_Sunlit)
%
% Where Moment = Failure Bending Moment, r = radius of boom, YS =
% Yield Stress of the boom material, Design_Efficiency = Fraction of
% boom material strength you want to use, SG = density of boom
% material, R = Specific Gas Constant of inflating gas, Temp_Shadow =
% temperature in shadow and Temp_Sunlit = temperature in sunlight.
%
% Some Rs... Air 287, Hydrogen 4130, Carbon Dioxide 189
%
% Example of a kapton-skinned hydrogen-filled boom:
% Boom(2,0.03,41000000,0.75,1.4,4130,123,470)
% -------------------------------------------------------------------
function Boom =
BOOM(Moment,r,YS,Design_Efficiency,SG,R,Temp_Shadow,Temp_Sunlit)
% Initialise variables
t = 0.00000001;
Efficiency = 1;
Iteration_Count = 0;
% Add thickness incrementally until material is working at an
acceptable
% efficiency
while (Efficiency > Design_Efficiency)
% Outer tube diameter
dout = 2*r;
% Inner tube diameter
din = (2*r) - (2*t);
% Moment of inertia
I = (pi*(dout^4 - din^4))/64;
% Calculate the maximum stress due to the applied bending moment
Sigma = Moment*r/I;
% Equate this to the Axial Stress due to pressure and solve for
pressure required in shadow,
% (minimum pressure condition) because the compression surface will
fail when Compressive Bending
% stress exceeds the Tensile Axial Stress
Pressure_shadow = Sigma*t*2/r;
% As the boom enters sunlight, assume temperature rises from
Temp_Shadow to
% (Temp_Sunlit + Temp_Shadow)/2. Rho, V and R remain constant
Pressure_sunlit = (Temp_Sunlit/Temp_Shadow)*Pressure_shadow;
% At maximum stress point on the tension surface, the Axial Stress is
Sigma
% + pressure Axial Stress
Axial_Stress = ((r-t)*Pressure_sunlit/2*t) + Sigma;
% And pressure Hoop Stress is...
Hoop_Stress = ((r-t)*Pressure_sunlit)/t;
% So equivalent stress is...
```

```
Von_Mises_Stress = sqrt((Axial_Stress^2) + (Hoop_Stress^2) -
Axial_Stress*Hoop_Stress);
% Material Strength Usage
Efficiency = Von_Mises_Stress/YS;
% Add increment of t
t = t + 0.00000001;
% Count
Iteration_Count = Iteration_Count + 1;
end
t
Boom_Mass_per_metre = 2*r*pi*t*SG;
Gas_Density = Pressure_sunlit/(R*Temp_Sunlit);
Gas_Mass_per_metre = pi*r*r*Gas_Density;
Total_Mass_per_metre = Boom_Mass_per_metre + Gas_Mass_per_metre
Percentage_of_which_is_gas =
(Gas_Mass_per_metre/Total_Mass_per_metre)*100
Pressure_sunlit_PSI = Pressure_sunlit*0.0001450377
Pressure_shadow_PSI = Pressure_shadow*0.0001450377
Iteration_Count
```

A2.2 *ConeTotal.m*

```
% CONETOTAL - A program to calculate the
% torques and forces due to atmospheric forces
% and SRP on a cone in LEO. The mass of the
% cone is considered to be concentrated at the apex.
% The convex surface is assumed to be silvered, the concave
% surface to be black.
%
% Call Syntax:
% ConeTotal(alt,area,theta,alphadot,opa)
%
% alt = altitude (km) area = area (m.m)
% theta = cone half-angle (rad)
% alphadot = pitch rate (rad/s), opa = opaquicity(0.001 - 0.999)
%
% -------------------------------------------------------------------
----
%
function ConeTotal = CONETOTAL(alt,area,theta,alphadot,opa)
alpha = 0;
while alpha < 3.2
alpha
% Calculate orbital parameters (rho estimated)
rho = (3.*10.^32)*((alt.*1000).^-7.8667);
SRP = 4.6.*10.^-6;
ref = opa;
abso = opa;
grav = 6.67.*10.^-11;
MoE = 5.98.*10.^24;
V = (grav.*MoE./(alt.*1000 + 6380000)).^0.5;
% Calculate cone parameters
length=sqrt((area./(pi.*sin(theta))));
r = length.*sin(theta);
axiallength = length.*cos(theta);
% Calculate flow parameters
beta = pi-alpha;
A = (sin(theta))*(cos(alpha));
B = (cos(theta))*(sin(alpha));
if (alpha~=0)
if (alpha~=pi)
psiL = acos(tan(theta)./tan(alpha));
end
end
% REGIME 1
if((alpha<=theta)&(alpha>=-theta))
Regime = 1;
%
% AERODYNAMIC
% Restoring Torque
aF1r = inline('((A - B.*cos(psi)).^2).*cos(psi)','psi','A','B');
aIntF1r = quad(aF1r,0,pi,[],[],A,B);
aRestoring = (2./3).*(length.^3).*sin(theta).*rho.*V.*V.*aIntF1r;
% Damping Torque
aF1d = inline('(A - B.*cos(psi)).*cos(psi).*cos(psi)','psi','A','B');
aIntF1d = quad(aF1d,0,pi,[],[],A,B);
aDamping = -(length.^4).*sin(theta).*rho.*V.*alphadot.*aIntF1d;
% Body Drag
aF1i = inline('((A - B.*cos(psi)).^2)','psi','A','B');
```

```
aIntF1i = quad(aF1i,0,pi,[],[],A,B);
aDrag = ((length.^2).*sin(theta).*sin(theta).*rho.*V.*V.*aIntF1i);
% Body Lift
aF1l = inline('((A - B.*cos(psi)).^2).*cos(psi)','psi','A','B');
aIntF1l = quad(aF1l,0,pi,[],[],A,B);
aLift = ((length.^2).*sin(theta).*cos(theta).*rho.*V.*V.*-aIntF1l);
%
% SRP - SPECULAR REFLECTION
% Restoring Torque
srF1r = inline('((A - B.*cos(psi)).^2).*cos(psi)','psi','A','B');
srIntF1r = quad(srF1r,0,pi,[],[],A,B);
srRestoring = (2./3).*(length.^3).*sin(theta).*2.*ref.*SRP.*srIntF1r;
% Body Drag
srF1i = inline('((A - B.*cos(psi)).^2)','psi','A','B');
srIntF1i = quad(srF1i,0,pi,[],[],A,B);
srDrag =
((length.^2).*sin(theta).*sin(theta).*2.*ref.*SRP.*srIntF1i);
% Body Lift
srF1l = inline('((A - B.*cos(psi)).^2).*cos(psi)','psi','A','B');
srIntF1l = quad(srF1l,0,pi,[],[],A,B);
srLift = ((length.^2).*sin(theta).*cos(theta).*2.*ref.*SRP.*-
srIntF1l);
%
% Results
Aero_Restoring_Torque = aRestoring;
Aero_Damping_Torque = aDamping;
Aero_Body_Drag = aDrag;
Aero_Body_Lift = aLift;
SRP_Restoring_Torque = srRestoring;
SRP_Body_Drag = srDrag;
SRP_Body_Lift = srLift;
%
% REGIME 2
elseif(((alpha>theta)&(alpha<=(pi/2))) | ((alpha<(-theta))&(alpha>=(-
pi/2))))
Regime = 2;
%
% AERODYNAMIC
% Restoring Torque
aF2r = inline('((A - B.*cos(psi)).^2).*cos(psi)','psi','A','B');
aIntF2r = quad(aF2r,psiL,pi,[],[],A,B);
aRestoring = (2./3).*(length.^3).*sin(theta).*rho.*V.*V.*aIntF2r;
% Damping Torque
aF2d = inline('(A - B.*cos(psi)).*cos(psi).*cos(psi)','psi','A','B');
aIntF2d = quad(aF2d,psiL,pi,[],[],A,B);
aDamping = -(length.^4).*sin(theta).*rho.*V.*alphadot.*aIntF2d;
% Body Drag
aF2i = inline('((A - B.*cos(psi)).^2)','psi','A','B');
aIntF2i = quad(aF2i,psiL,pi,[],[],A,B);
aDrag = ((length.^2).*sin(theta).*sin(theta).*rho.*V.*V.*aIntF2i);
% Body Lift
aF2l = inline('((A - B.*cos(psi)).^2).*cos(psi)','psi','A','B');
aIntF2l = quad(aF2l,psiL,pi,[],[],A,B);
aLift = ((length.^2).*sin(theta).*cos(theta).*rho.*V.*V.*-aIntF2l);
%
% SRP - SPECULAR REFLECTION
% Restoring Torque
srF2r = inline('((A - B.*cos(psi)).^2).*cos(psi)','psi','A','B');
srIntF2r = quad(srF2r,psiL,pi,[],[],A,B);
```

```
srRestoring = (2./3).*(length.^3).*sin(theta).*2.*ref.*SRP.*srIntF2r;
% Body Drag
srF2i = inline('((A - B.*cos(psi)).^2)','psi','A','B');
srIntF2i = quad(srF2i,psiL,pi,[],[],A,B);
srDrag =
((length.^2).*sin(theta).*sin(theta).*2.*ref.*SRP.*srIntF2i);
% Body Lift
srF2l = inline('((A - B.*cos(psi)).^2).*cos(psi)','psi','A','B');
srIntF2l = quad(srF2l,psiL,pi,[],[],A,B);
srLift = ((length.^2).*sin(theta).*cos(theta).*2.*ref.*SRP.*-
srIntF2l);
% Results
Aero_Restoring_Torque = aRestoring;
Aero_Damping_Torque = aDamping;
Aero_Body_Drag = aDrag;
Aero_Body_Lift = aLift;
SRP_Restoring_Torque = srRestoring;
SRP_Body_Drag = srDrag;
SRP_Body_Lift = srLift;
%
% REGIME 3
elseif(((alpha<(pi-theta))&(alpha>(pi/2))) | ((alpha>(-
pi+theta))&(alpha<(-pi/2))))
Regime = 3;
%
% OUTSIDE
% AERODYNAMIC
% Restoring Torque
aF3ro = inline('((A - B.*cos(psi)).^2).*cos(psi)','psi','A','B');
aIntF3ro = quad(aF3ro,psiL,pi,[],[],A,B);
aRestoring_Out =
(2./3).*(length.^3).*sin(theta).*rho.*V.*V.*aIntF3ro;
% Damping Torque
aF3do = inline('(A -
B.*cos(psi)).*cos(psi).*cos(psi)','psi','A','B');
aIntF3do = quad(aF3do,psiL,pi,[],[],A,B);
aDamping_Out = -(length.^4).*sin(theta).*rho.*V.*alphadot.*aIntF3do;
% Body Drag
aF3io = inline('((A - B.*cos(psi)).^2)','psi','A','B');
aIntF3io = quad(aF3io,psiL,pi,[],[],A,B);
aDrag_Out =
((length.^2).*sin(theta).*sin(theta).*rho.*V.*V.*aIntF3io);
% Lift Force
aF3lo = inline('((A - B.*cos(psi)).^2).*cos(psi)','psi','A','B');
aIntF3lo = quad(aF3lo,psiL,pi,[],[],A,B);
aLift_Out = ((length.^2).*sin(theta).*cos(theta).*rho.*V.*V.*-
aIntF3lo);
%
% SRP - SPECULAR REFLECTION
% Restoring Torque
srF3ro = inline('((A - B.*cos(psi)).^2).*cos(psi)','psi','A','B');
srIntF3ro = quad(srF3ro,psiL,pi,[],[],A,B);
srRestoring_Out =
(2./3).*(length.^3).*sin(theta).*2.*ref.*SRP.*srIntF3ro;
% Body Drag
srF3io = inline('((A - B.*cos(psi)).^2)','psi','A','B');
srIntF3io = quad(srF3io,psiL,pi,[],[],A,B);
srDrag_Out =
((length.^2).*sin(theta).*sin(theta).*2.*ref.*SRP.*srIntF3io);
```

```
% Body Lift
srF3lo = inline('((A - B.*cos(psi)).^2).*cos(psi)','psi','A','B');
srIntF3lo = quad(srF3lo,psiL,pi,[],[],A,B);
srLift_Out = ((length.^2).*sin(theta).*cos(theta).*2.*ref.*SRP.*-
srIntF3lo);
%
% Outside Results
Aero_Restoring_Torque_Out = aRestoring_Out;
Aero_Damping_Torque_Out = aDamping_Out;
Aero_Body_Drag_Out = aDrag_Out;
Aero_Body_Lift_Out = aLift_Out;
SRP_Restoring_Torque_Out = srRestoring_Out;
SRP_Body_Drag_Out = srDrag_Out;
SRP_Body_Lift_Out = srLift_Out;
%
% INSIDE
% AERODYNAMIC
% Restoring Torque
aF3ri = inline('((s.^2).*(((A -
B.*cos(psi)).^2).*cos(psi))).*((s)>(length.*(sin(acos((-(-2.*(-
((axiallength.*sin(beta))./r)).*(cos(beta)))   -   ((((-2.*(-
((axiallength.*sin(beta))./r)).*(cos(beta))).^2) - 4.*((-
(((cos(beta)).*axiallength.*(tan(beta)))./(r.*sin(psi)) +
(cos(beta).*(cos(psi))./(sin(psi))))).^2 + ((cos(beta)).^2)).*(((-
((axiallength.*sin(beta))./r)).^2) - ((-
(((cos(beta)).*axiallength.*(tan(beta)))./(r.*sin(psi)) +
(cos(beta).*(cos(psi))./(sin(psi))))).^2))).^0.5))./(2.*(((-
(((cos(beta)).*axiallength.*(tan(beta)))./(r.*sin(psi)) +
(cos(beta).*(cos(psi))./(sin(psi))))).^2) +
((cos(beta)).^2))))))./(sin(psi))))','psi','s','A','B','length','axia
llength','beta','r');
aIntF3ri =
dblquad(aF3ri,0.0001,psiL,0,length,[],[],A,B,length,axiallength,beta,
r);
aRestoring_In = - 2.*sin(theta).*rho.*V.*V.*aIntF3ri;
% Damping Torque
aF3di = inline('((s.^3).*(A -
B.*cos(psi)).*cos(psi).*cos(psi)).*((s)>(length.*(sin(acos((-(-2.*(-
((axiallength.*sin(beta))./r)).*(cos(beta)))   -   ((((-2.*(-
((axiallength.*sin(beta))./r)).*(cos(beta))).^2) - 4.*((-
(((cos(beta)).*axiallength.*(tan(beta)))./(r.*sin(psi)) +
(cos(beta).*(cos(psi))./(sin(psi))))).^2 + ((cos(beta)).^2)).*(((-
((axiallength.*sin(beta))./r)).^2) - ((-
(((cos(beta)).*axiallength.*(tan(beta)))./(r.*sin(psi)) +
(cos(beta).*(cos(psi))./(sin(psi))))).^2))).^0.5))./(2.*(((-
(((cos(beta)).*axiallength.*(tan(beta)))./(r.*sin(psi)) +
(cos(beta).*(cos(psi))./(sin(psi))))).^2) +
((cos(beta)).^2))))))./(sin(psi))))','psi','s','A','B','length','axia
llength','beta','r');
aIntF3di =
dblquad(aF3di,0.0001,psiL,0,length,[],[],A,B,length,axiallength,beta,
r);
aDamping_In = 4.*sin(theta).*rho.*V.*alphadot.*aIntF3di;
% Body Drag
aF3ii = inline('((s).*((A -
B.*cos(psi)).^2)).*((s)>(length.*(sin(acos((-(-2.*(-
((axiallength.*sin(beta))./r)).*(cos(beta)))   -   ((((-2.*(-
((axiallength.*sin(beta))./r)).*(cos(beta))).^2) - 4.*((-
(((cos(beta)).*axiallength.*(tan(beta)))./(r.*sin(psi)) +
```

```
(cos(beta).*(cos(psi))./(sin(psi))))).^2 + ((cos(beta)).^2)).*(((-
((axiallength.*sin(beta))./r)).^2) - ((-
(((cos(beta)).*axiallength.*(tan(beta)))./(r.*sin(psi)) +
(cos(beta).*(cos(psi))./(sin(psi))))).^2))).^0.5))./(2.*(((-
(((cos(beta)).*axiallength.*(tan(beta)))./(r.*sin(psi)) +
(cos(beta).*(cos(psi))./(sin(psi))))).^2) +
((cos(beta)).^2))))))./(sin(psi))))','psi','s','A','B','length','axia
llength','beta','r');
aIntF3ii =
dblquad(aF3ii,0.0001,psiL,0,length,[],[],A,B,length,axiallength,beta,
r);
aDrag_In = - (2.*sin(theta).*sin(theta).*rho.*V.*V.*aIntF3ii);
% Body Lift
aF3li = inline('((s).*((A -
B.*cos(psi)).^2).*cos(psi)).*((s)>(length.*(sin(acos((-(-2.*(-
((axiallength.*sin(beta))./r)).*(cos(beta)))   -   ((((-2.*(-
((axiallength.*sin(beta))./r)).*(cos(beta))).^2) - 4.*((-
(((cos(beta)).*axiallength.*(tan(beta)))./(r.*sin(psi)) +
(cos(beta).*(cos(psi))./(sin(psi))))).^2 + ((cos(beta)).^2)).*(((-
((axiallength.*sin(beta))./r)).^2) - ((-
(((cos(beta)).*axiallength.*(tan(beta)))./(r.*sin(psi)) +
(cos(beta).*(cos(psi))./(sin(psi))))).^2))).^0.5))./(2.*(((-
(((cos(beta)).*axiallength.*(tan(beta)))./(r.*sin(psi)) +
(cos(beta).*(cos(psi))./(sin(psi))))).^2) +
((cos(beta)).^2))))))./(sin(psi))))','psi','s','A','B','length','axia
llength','beta','r');
aIntF3li =
dblquad(aF3li,0.0001,psiL,0,length,[],[],A,B,length,axiallength,beta,
r);
aLift_In = - (2.*sin(theta).*cos(theta).*rho.*V.*V.*-aIntF3li);
%
% SRP - TOTAL ABSORPTION
% Restoring Torque
AreaOpen = pi.*r.*r.*cos(beta);
OpenForce = abso.*SRP.*AreaOpen;
MomentArm = axiallength.*sin(beta);
saRestoring_In = -OpenForce.*MomentArm;
% Body Drag
saDrag_In = -OpenForce.*cos(beta);
% Body Lift
saLift_In = OpenForce.*sin(beta);
%
% Inside Results
Aero_Restoring_Torque_In = aRestoring_In;
Aero_Damping_Torque_In = aDamping_In;
Aero_Body_Drag_In = aDrag_In;
Aero_Body_Lift_In = aLift_In;
SRP_Restoring_Torque_In = saRestoring_In;
SRP_Body_Drag_In = saDrag_In;
SRP_Body_Lift_In = saLift_In;
%
% Results
Aero_Restoring_Torque = Aero_Restoring_Torque_Out +
Aero_Restoring_Torque_In;
Aero_Damping_Torque = Aero_Damping_Torque_Out +
Aero_Damping_Torque_In;
Aero_Body_Drag = Aero_Body_Drag_Out + Aero_Body_Drag_In;
Aero_Body_Lift = Aero_Body_Lift_Out + Aero_Body_Lift_In;
```

```
SRP_Restoring_Torque = SRP_Restoring_Torque_Out +
SRP_Restoring_Torque_In;
SRP_Body_Drag = SRP_Body_Drag_Out + SRP_Body_Drag_In;
SRP_Body_Lift = SRP_Body_Lift_Out + SRP_Body_Lift_In;
%
% REGIME 4
else
Regime = 4;
%
% AERODYNAMIC
% Restoring Torque
aF4r = inline('((A - B.*cos(psi)).^2).*cos(psi)','psi','A','B');
aIntF4r = quad(aF4r,0,pi,[],[],A,B);
aRestoring = - (2./3).*(length.^3).*sin(theta).*rho.*V.*V.*aIntF4r;
% Damping Torque
aF4d = inline('(A - B.*cos(psi)).*cos(psi).*cos(psi)','psi','A','B');
aIntF4d = quad(aF4d,0,pi,[],[],A,B);
aDamping = (length.^4).*sin(theta).*rho.*V.*alphadot.*aIntF4d;
% Drag Force
aF4i = inline('((A - B.*cos(psi)).^2)','psi','A','B');
aIntF4i = quad(aF4i,0,pi,[],[],A,B);
aDrag = - ((length.^2).*sin(theta).*sin(theta).*rho.*V.*V.*aIntF4i);
% Lift Force
aF4l = inline('((A - B.*cos(psi)).^2).*cos(psi)','psi','A','B');
aIntF4l = quad(aF4l,0,pi,[],[],A,B);
aLift = - ((length.^2).*sin(theta).*cos(theta).*rho.*V.*V.*-aIntF4l);
%
% SRP - TOTAL ABSORPTION
% Restoring Torque
AreaOpen = pi.*r.*r.*cos(beta);
OpenForce = abso.*SRP.*AreaOpen;
MomentArm = axiallength.*sin(beta);
saRestoring = -OpenForce.*MomentArm;
% Body Drag
saDrag = -OpenForce.*cos(beta);
% Body Lift
saLift = OpenForce.*sin(beta);
%
% Results
Aero_Restoring_Torque = aRestoring;
Aero_Damping_Torque = aDamping;
Aero_Body_Drag = aDrag;
Aero_Body_Lift = aLift;
SRP_Restoring_Torque = saRestoring;
SRP_Body_Drag = saDrag;
SRP_Body_Lift = saLift;
end
%
% QUOTIENTS
ARQ = Aero_Restoring_Torque./(rho.*V.*V);
ADQ = Aero_Damping_Torque./(rho.*V.*alphadot);
ABD = Aero_Body_Drag/(rho.*V.*V);
ABL = Aero_Body_Lift/(rho.*V.*V);
SRRQ = SRP_Restoring_Torque./(opa.*SRP);
SRBD = SRP_Body_Drag./(opa.*SRP);
SRBL = SRP_Body_Lift./(opa.*SRP);
%
i = 10.*alpha;
%
```

```
quotient(1,round(i+1))=ARQ;
quotient(2,round(i+1))=ADQ;
quotient(3,round(i+1))=ABD;
quotient(4,round(i+1))=ABL;
quotient(5,round(i+1))=SRRQ;
quotient(6,round(i+1))=SRBD;
quotient(7,round(i+1))=SRBL;
%
alpha = alpha + 0.1;
end
csvwrite('Quotients.csv',quotient)
```

A2.3 *Deflect.m*

```
% DEFLECT - A program developed to calculate the deflection of
% the struts on a deorbit device
%
% Call Syntax:
% deflect(Mu,L,Theta,EI)
%
% -------------------------------------------------------------------
function deflect = deflect(Mu,L,Theta,EI)
End_S = L.*sin(Theta).*cos(pi./4);
End_D = L;
Count2 = 1;
while (Count2 < 9)
d_eff_boom = atan(End_D./L);
ThetaBoom = (Theta) - d_eff_boom;
End_X_undeflected = End_S;
End_X_deflected = (L.*sin(Theta - d_eff_boom)).*cos(pi./4);
Count = 1;
Psi = 1;
while (Count < 100000)
    Psi = acot(((End_S.*Mu).*(log(tan(Psi./2))))./-
    (Mu.*End_X_deflected));
    Count = Count + 1;
end
Psi;
End_Y_deflected = (End_X_deflected.*(-log(sin(Psi))))./((pi./2)-Psi);
d_eff_web = atan(End_Y_deflected./End_S);
ThetaWeb = atan(End_S./(L.*cos(Theta)));
Theta_eff = ((Theta - d_eff_boom) + (ThetaWeb - d_eff_web))./2;
Mu_eff = Mu.*sin(Theta_eff);
End_T = 1./((1./(Mu_eff.*End_X_deflected)).*((pi./2) - Psi));
End_F = 2.*End_T.*cos(pi./4).*sin(Psi);
P = 0.5.*End_F.*L;
Qo = 2.*End_T.*cos(pi./4).*cos(Psi);
k = sqrt(P./(EI));
C1 = cos(k.*L);
C2 = sin(k.*L);
CA3 = 1 - cos(k.*L);
CA4 = (k.*L) - sin(k.*L);
CA5 = (((k.^2).*(L.^2))./2) - CA3;
CA6 = (((k.^3).*(L.^3))./6) - CA4;
y = ((-Qo./((k.^2).*P))*((C2.*CA4 - C1.*CA5)./C1)) -
((-Qo./((k.^3).*P.*L)).*((C2.*CA5 - C1.*CA6)./C1));
if (y > 0)
disp('Super-buckling load. Aborting...')
break
else
End_D = abs(y);
Count2 = Count2 + 1;
end
end
Area_Proj = (2.*End_S)^2
Def = End_D./L
```

Appendix 3 – Simulink mdl-files

A3.1 *Equatorial_Plane.mdl*

This version of *Equatorial_Plane.mdl* has been set up to run 50 simulations in parallel, and, to prevent clashes arising from signal dimension mismatches, it was necessary to have 50 versions of the MSIS-90 Look-Up Table. These are truncated at the right.

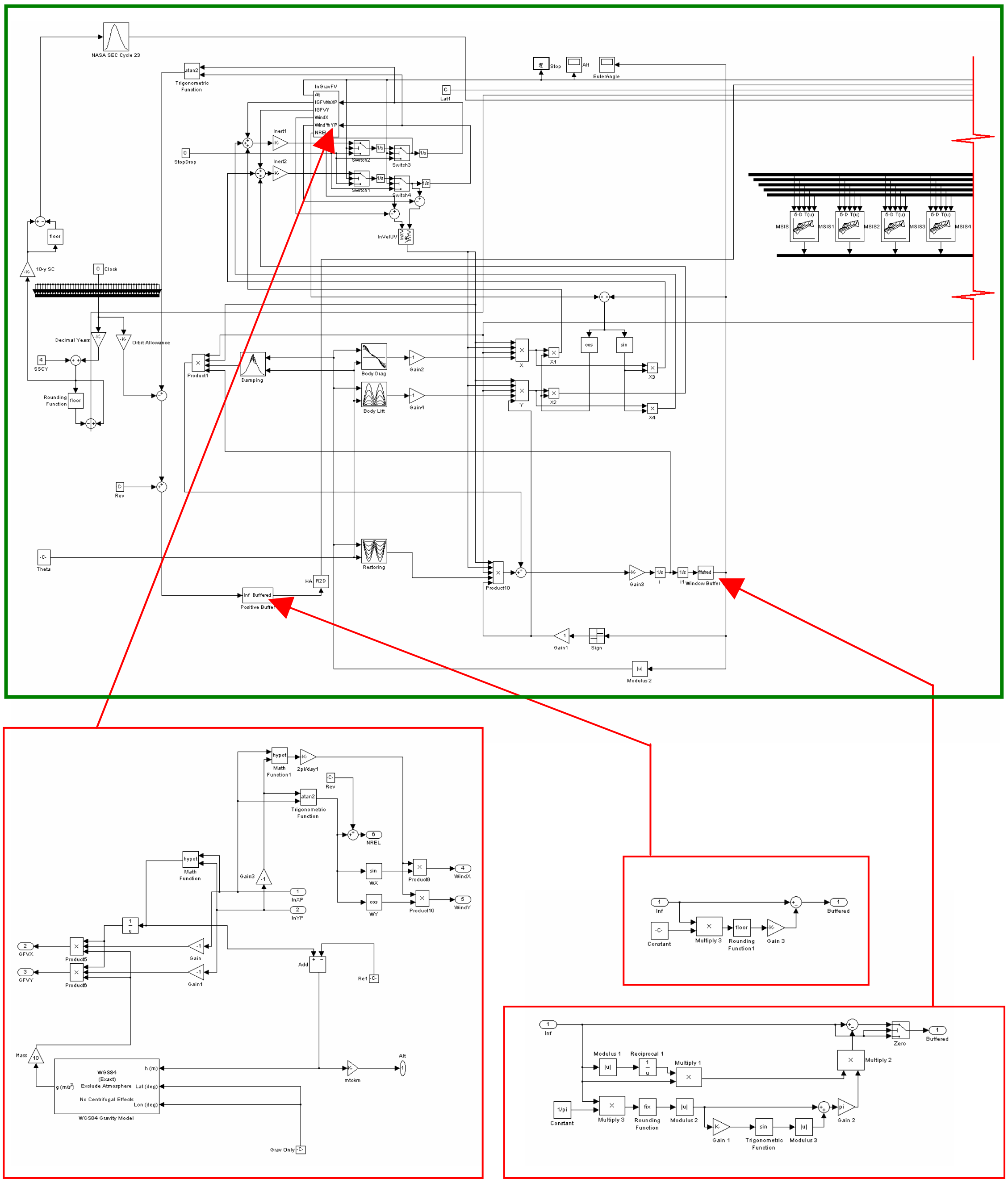

A3.2 *Six_DOF.mdl*

Blocks entitled 'Positive Buffer' and 'Window Buffer' contain the same routing as their counterparts in *Equatorial_Plane.mdl.*

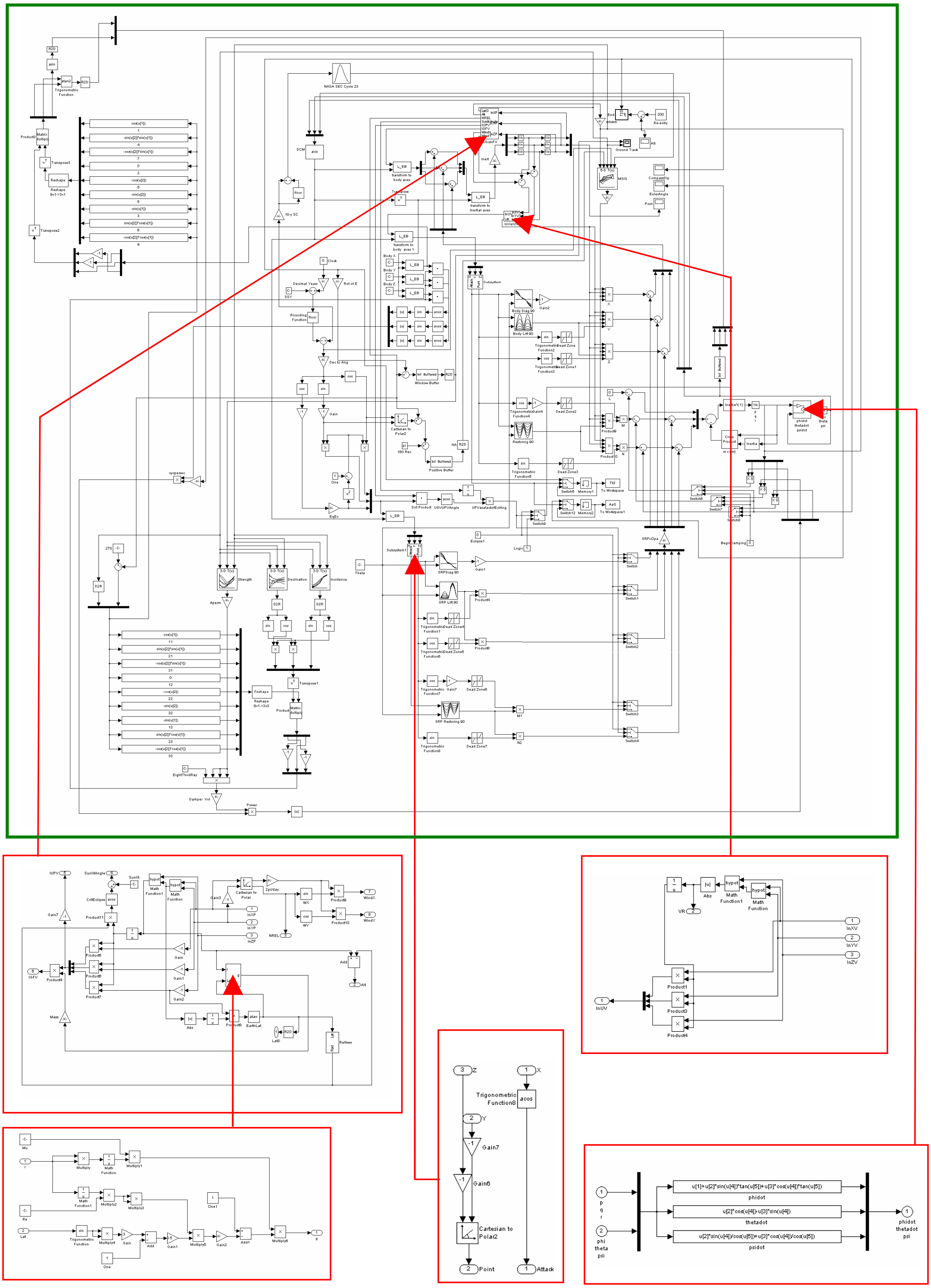

A3.3 *Reentry.mdl*

Blocks entitled 'X' are simply signal crossovers.

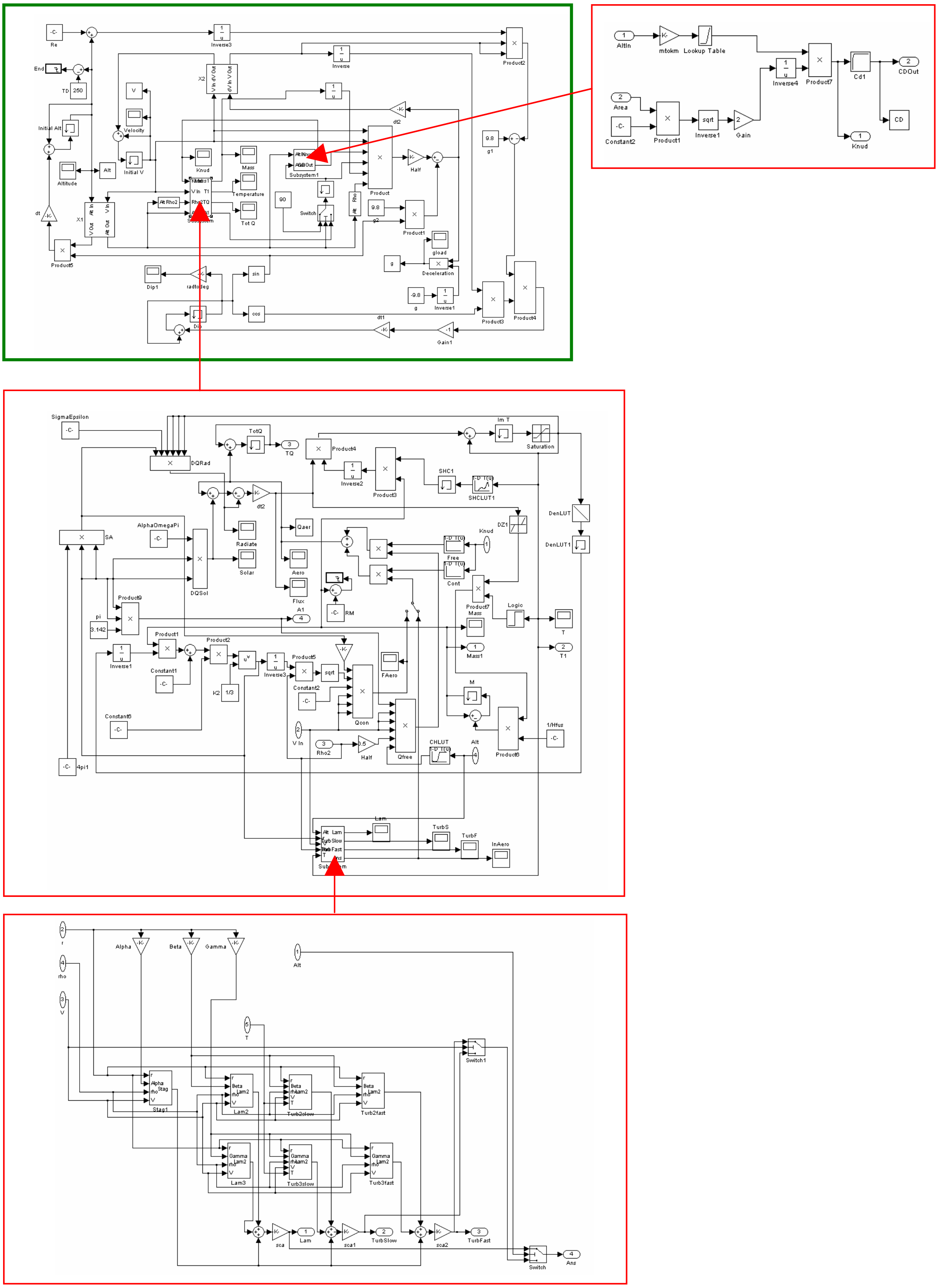

Appendix 4 – Large Demonstrators

It was discovered during the construction of the practical demonstrators that solid NiTiNOL elements with diameters of a few millimetres cannot be cantilevered more than about 0.5 m from the central hub before they sag under gravity. This is not a problem in space, but it does make the Earth-bound investigation of the different deployment mechanisms very difficult.

NiTiNOL is available in a stiffer tubular form, but the cost is perhaps 100 times greater than for solid elements. Therefore, an alternative method was developed to construct larger demonstrators. This involved using five NiTiNOL elements braced in parallel by lightweight nodes. During the service flexion of the structure large stresses are placed upon the nodes, and so after failed experiments with cork, butyl and acrylic, aluminium shim washers obtained from Bombardier Aerospace (Shorts) were found to be suitable.

Methods of bonding the NiTiNOL to the nodes investigated included super-gluing, resin and putty epoxying, JB-welding, soldering and brazing, but in all cases the flexion of the structure caused the joints to fail. Ultimately, only slow-cure Araldite was found to be effective, and even so failure is increasingly likely after 10 – 20 flexions of the structure.

Despite these difficulties, the cantileverable range of the NiTiNOL elements was extended to approximately 1.2 metres.

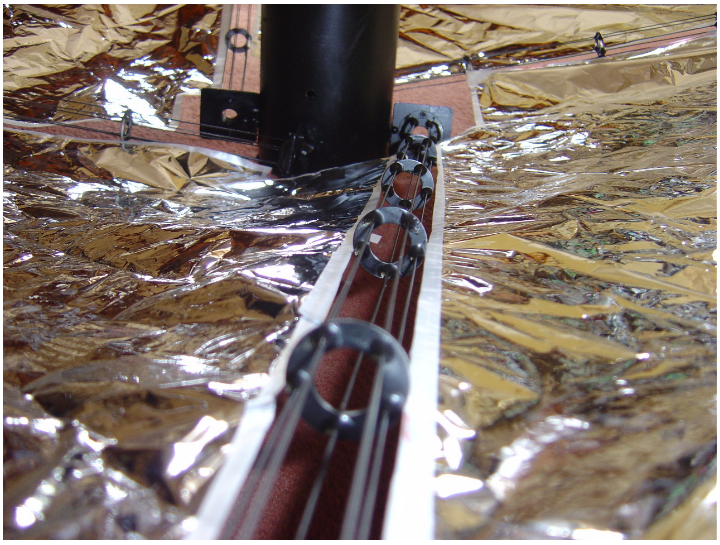

Figure A4-1 Detail of the five-core NiTiNOL booms developed for larger demonstrators. The aluminium shim washers and the Araldite bonds are visible under the black primer which was applied to aid photography.

Appendix 5 – Design Tools and Product Information

A5.1 ADAM

The ADAM booms supplied by Able Engineering Inc. may be sized by means of this design tool, sourced from their website at aec-able.com (2006).

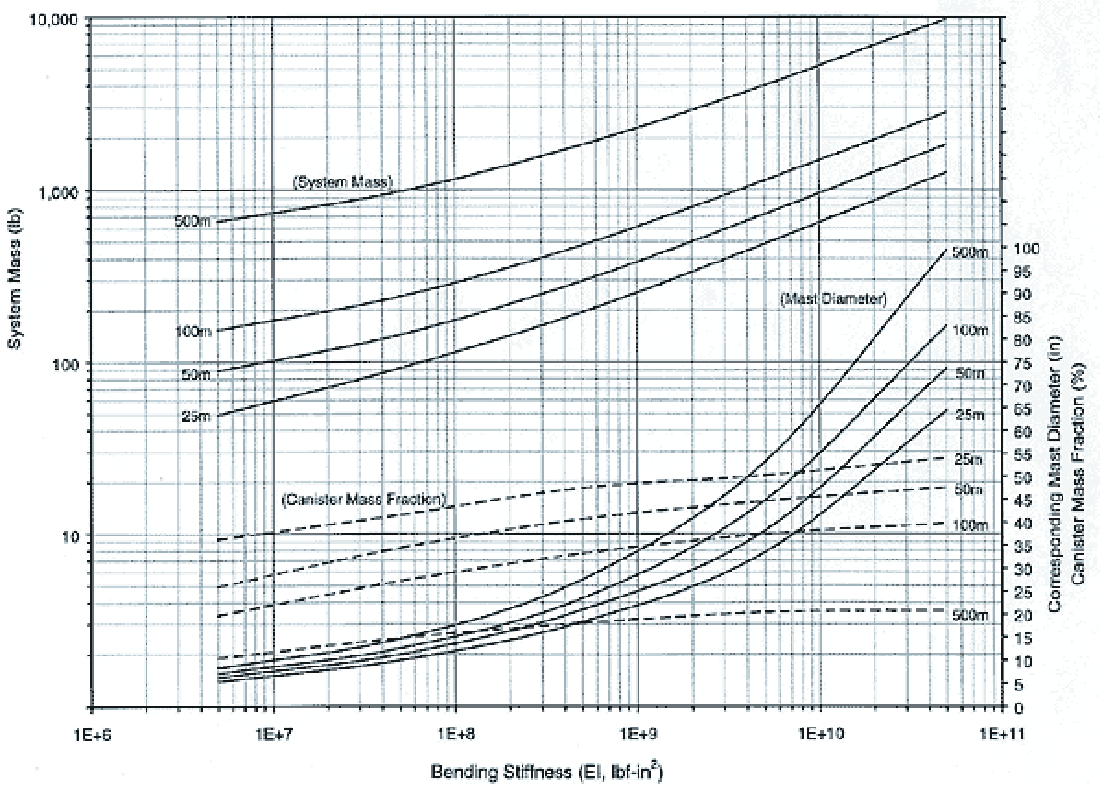

Figure A5-1 ADAM boom design tool, supplied by Able Engineering Inc.

A5.2 STEMs

The STEM systems shown here have been obtained from the Northrop Grumman website (northropgrumman.com (2006)).

A5.2.1 STEM JIB

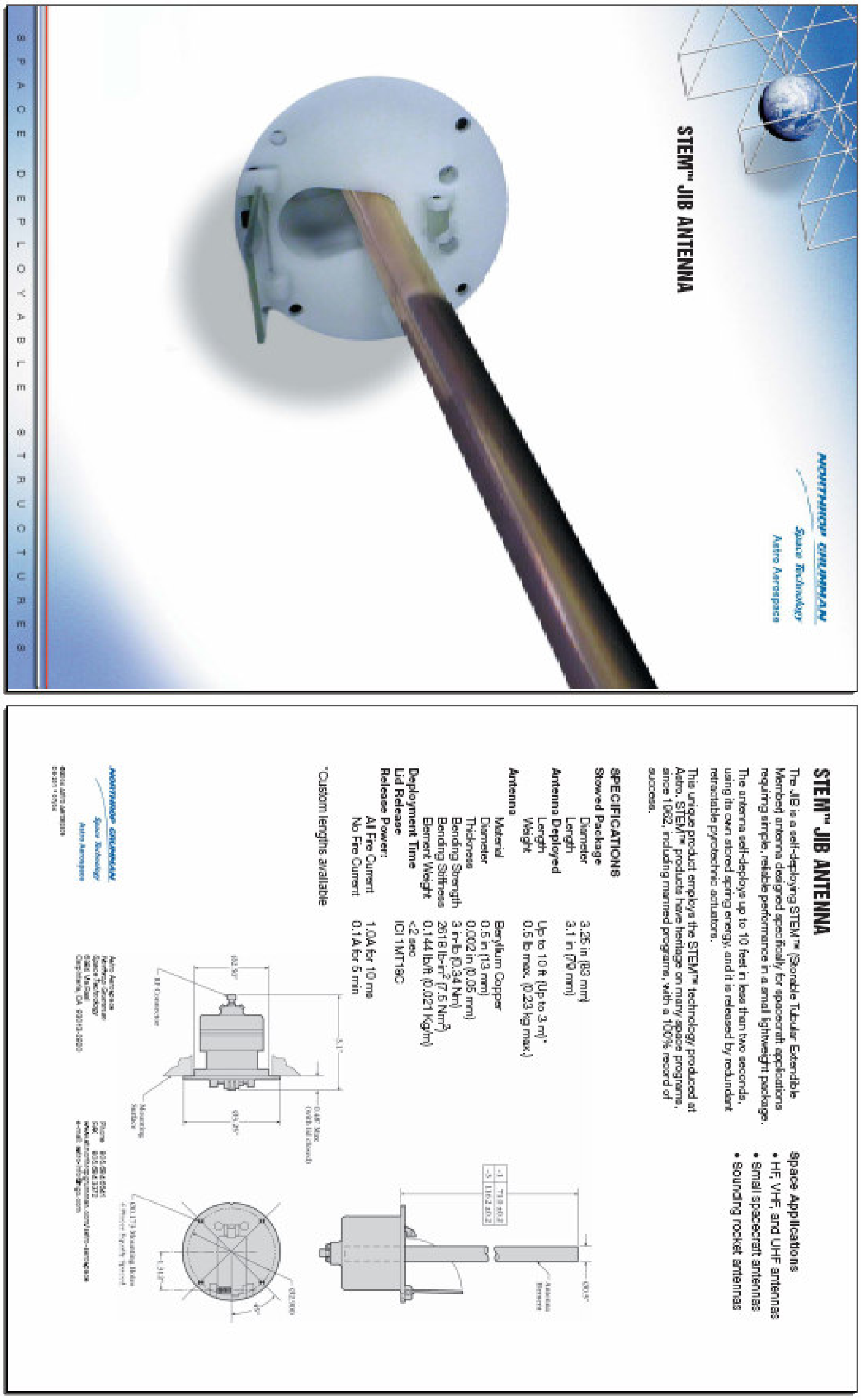

Figure A5-2 STEM JIB data sheet, supplied by Northrop Grumman Inc.

A5.2.2 TIP DRUM

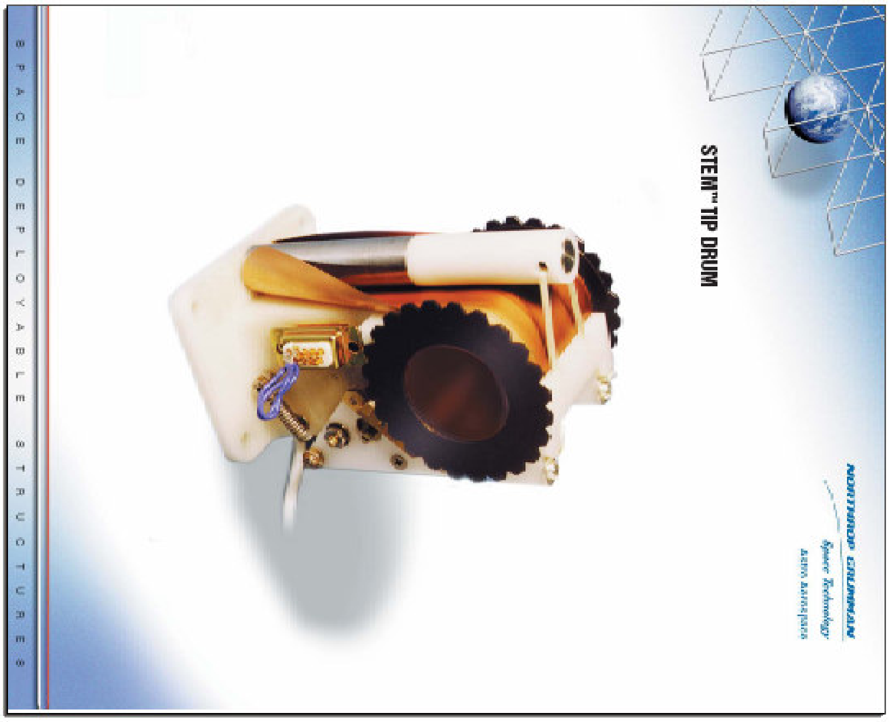

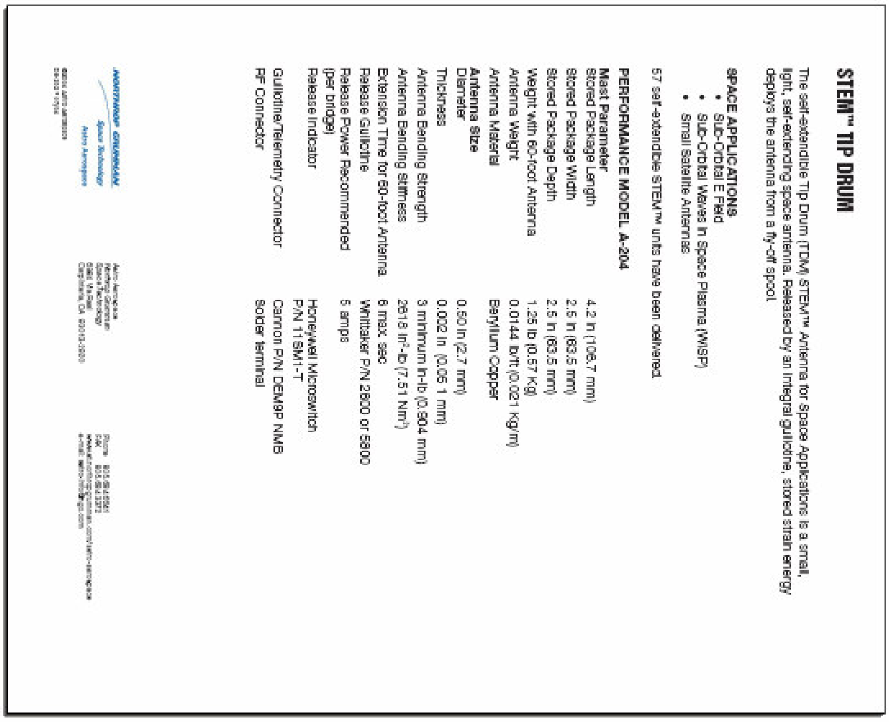

STEM™ TIP DRUM

The self-extendible Tip Drum (TDM) STEM™ Antenna for Space Applications is a small, light, self-extending space antenna. Released by an integral guillotine, stored strain energy deploys the antenna from a fly-off spool.

SPACE APPLICATIONS
- Sub-Orbital E Field
- Sub-Orbital Waves in Space Plasma (WISP)
- Small Satellite Antennas

57 self-extendible STEM™ units have been delivered.

PERFORMANCE MODEL A-204

Mast Parameter	
Stored Package Length	4.2 in (106.7 mm)
Stored Package Width	2.5 in (63.5 mm)
Stored Package Depth	2.5 in (63.5 mm)
Weight with 60-foot Antenna	1.25 lb (0.57 Kg)
Antenna Weight	0.0144 lb/ft (0.021 Kg/m)
Antenna Material	Beryllium Copper
Antenna Size	
Diameter	0.50 in (2.7 mm)
Thickness	0.002 in (0.05 1 mm)
Antenna Bending Strength	3 minimum in-lb (0.904 mm)
Antenna Bending stiffness	2618 in²-lb (7.51 Nm²)
Extension Time for 60-foot Antenna	6 max. sec
Release Guillotine	Whittaker P/N 2800 or 5800
Release Power Recommended (per bridge)	5 amps
Release Indicator	Honeywell Microswitch P/N 11SM1-T
Guillotine/Telemetry Connector	Cannon P/N DEM9P NMB
RF Connector	Solder terminal

NORTHROP GRUMMAN
Space Technology
Astro Aerospace

Figure A5-3 TIP DRUM data sheet, supplied by Northrop Grumman Inc.

A5.2.3 MICROSAT

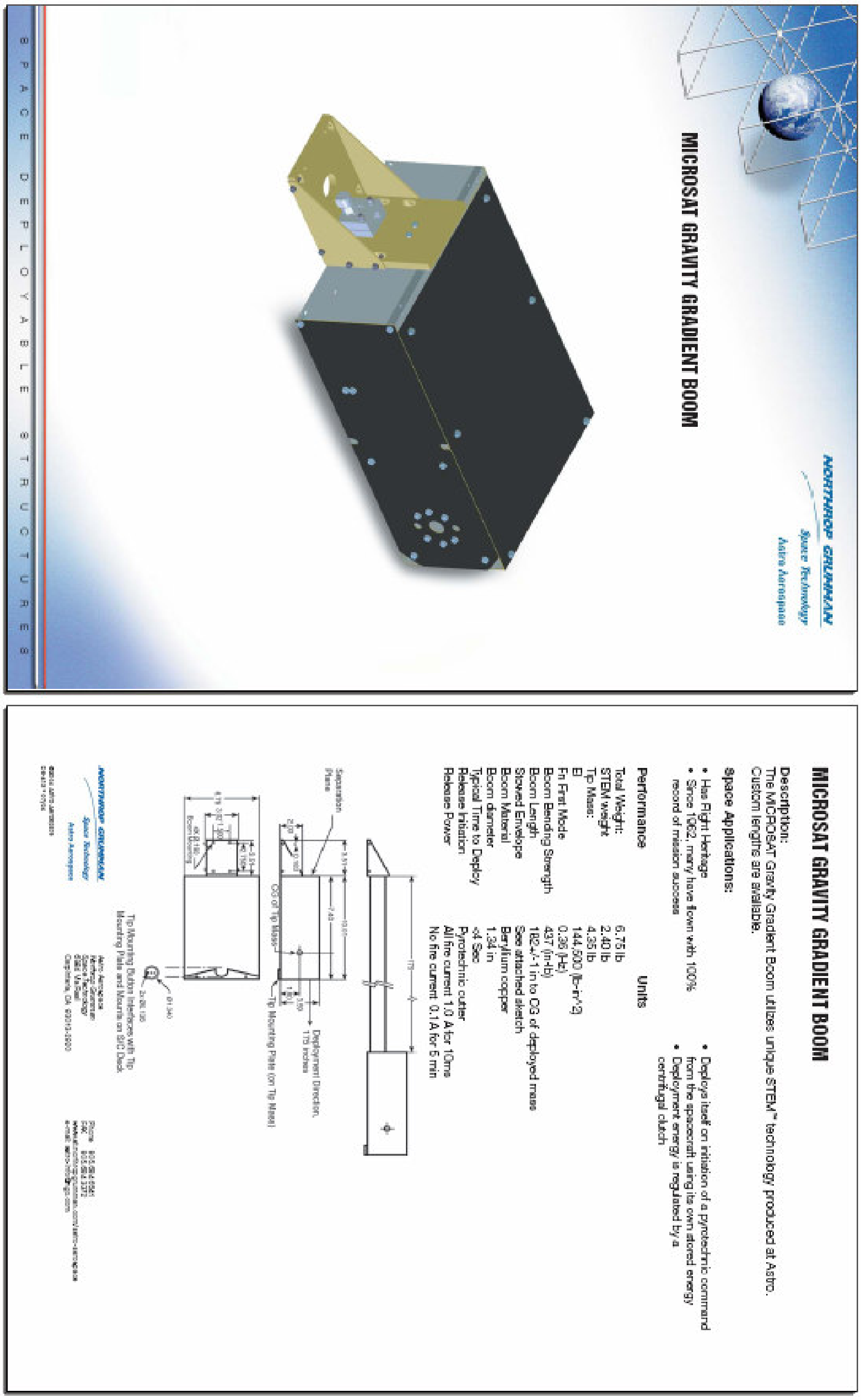

Figure A5-4 MICROSAT data sheet, supplied by Northrop Grumman Inc.

A5.2.4 BI-STEM

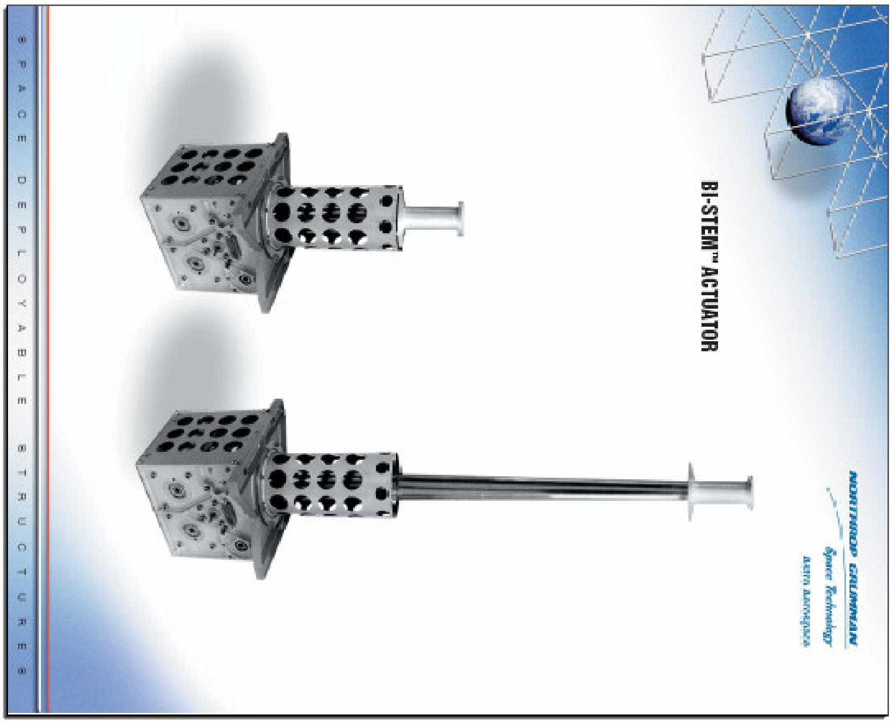

BI-STEM™ ACTUATOR

Designed for use as an actuator or instrument boom, the BI-STEM™ deploys and retracts a 0.86-inch (22 mm) diameter BI-STEM™ in lengths adjustable up to 20 feet (6 meters) against a rated compressive load of 5 lb (22 n).

The Model 2646, as shown was developed from the Hubble Space Telescope solar array actuator and is qualified for space applications.

A DC motor drives the actuator which also includes limit switches to terminate and indicate complete deployment or retraction. Length indication is provided in analog form by a potentiometer.

SPACE APPLICATIONS

- Developed from Hubble Space Telescope Solar Array Deployer
- Skynet IV UHF Antenna Deployment Actuator, Model 2646 (as shown)
- Viking Langmuir Probe Instrument Boom, Model 2646

PERFORMANCE

Actuator Size	
Height	9.84 in (250 mm)
Width	5.00 in (127 mm)
Depth	3.98 in (101 mm)
Depth (Optional Mounting Plate)	6.00 in (152.4 mm)
Actuator Weight (without boom)	3.53 lb (1.6 Kg)
Boom Weight	0.09 lb/ft (0.134 Kg/m)
Boom Material	Stainless Steel or Beryllium Copper
Boom Coating	Kapton Coat/Kapton Tape
Boom Properties for Stainless Steel	
Min. Bending Stiffness	45,650 lb-in² (131 nm²)
Allowable Compressive Load	5 lb (22 n)
Ultimate Bending Strength	239 in-lb (27 nm)
Deployment Rate (nominal)	1 in/s (25 mm/sec)
Drive Motor	DC Permanent Magnet Brush Type
Power Requirements (Max at 28 V DC)	15 watts
Limit Switches	2 for Full Deployment; 1 for Full Retraction
Length Indication (Potentiometer)	10,000 ohms
Interface Connector	Cannon Dam-15P-NMB-K56
Environmental	Qualified for Ariane launch
Random Vibration	19.5 g Rms
Stowed Frequency	>50 Hz
Operating Temperature Limits	Qualified at -20 to +60°C

NORTHROP GRUMMAN
Space Technology
Astro Aerospace

Astro Aerospace
Northrop Grumman
Space Technology

Figure A5-5 BI-STEM data sheet, supplied by Northrop Grumman Inc.

A5.3 CTMs

This information regarding CTMs has been obtained from the literature of SENER Ingeniera Y Sistemas, *via* the research of Broughton (2003).

Collapsible Tubular Mast (CTM)

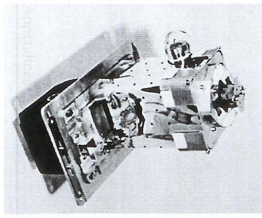

Collapsible Tube Mast

SENER Ingeniera Y Sistemas

Spacecraft Bus

Structures & Mechanisms

Mechanical Components

Description

The CTM is a biconvex tube mast that can be flattened and then rolled up around a drum into a small volume package. A drive system pulls the tube by the edge to deploy, and rotates the drum to retract. This approach leads to a mast fully operational and backlash free at any intermediary position, from zero to fully deployed. The mast can be manufactured in metal and composite (CRFP), in both cases a continuous manufacturing method is used, then, it provides tubes of unlimited length. The CTM design has been performed in a flexible way to provide scalable sizes to be compatible with each specific customer requirements. A flat cable can be implemented also in the mast to provide signal and power to any payloads/experiments placed on the top.

Features

Mast Size		1	2	3	4	5
Height (mm) Width (mm)		22 31	43 60	63 88	93 132	133 194
Mass (g/m)	BeCu CFRP	34 -	135 -	298 55	590 110	1070 180
Elx (Nm^2) (Bending stiff.)	BeCu CFRP	21 -	338 -	1584 490	6579 3136	24800 11200
Ely (Nm2) (Bending stiff.)	BeCu CFRP	38 -	581 -	2787 1060	11890 6785	44700 21700
GJ (Nm2) (Tor. stiff.)	BeCu CFRP	10 -	166 -	777 49	3315 313	12200 1100
Mcr. (Nm) (Critical bending moment)	BeCu CFRP	2 -	17 -	58 20	165 55	550 150
Length (m)	Only limited by external requirements					
Deployment Mechanism						
Dimensions (mm)	W x B L	104 x 73 188	190 x 135 375	250 x 178 570	370 x 264 844	500 x 356 1158
Mass (kg)		1	3	6	-	-

Application Fields

Small sizes: monopole or dipole antenna (e.g. Ulysses).
Medium sizes: deploy small to medium size scientific payloads (e.g. magnetometers)
Large sizes: deploy large payloads as scientific experiments, large size of solar array.

State of the Art

The CTM provides important advantage over the current state of the art. Significant improvement of strength and stiffness has been obtained, maintaining at the same time a small stowed volume and simple interface. The high number of size alternatives gives also an important advantage to reach an optimum design for each customer requirements.

Availability

This product is commercially available. It can be adapted upon request for customer specific applications. The Mast can be delivered with different configurations including or not the following units: drive electronics, flat cable, thermal protection.

Contact

SENER Ingeniera Y Sistemas
Mr Alvaro AZCARRAGUA ARANA
Managing Director
Tel +34 91 807 71 60
Fax +34 91 807 72 09
alvaro.azcarraga@sener.es
C/Severo Ochoa 4
E-28760 Tres Cantos- Madrid

SENER

Figure A5-6 CTM data sheet, reproduced from Broughton (2003)

A5.4 Telescopic Masts

The Telescopic Masts shown here have been obtained from the Northrop Grumman website (northropgrumman.com (2006)).

TELESCOPIC MAST MODEL 7301

DESCRIPTION

The Astro Telescopic Mast (Patent No. 5,315,795) is light and volume efficient. It locks in place when deployed and can be provided with a retractability feature. This mast is easily sized to fit various stowed envelopes, stiffnesses and strengths, based on specific needs. The materials suitable for the mast include aluminum, steel, fiberglass, graphite/epoxy and carbon-carbon.

SPACE APPLICATIONS

- Deployable booms for spacecraft
- Separator for spacecraft payloads
- Solar array blanket support

SPECIFICATIONS

Mast Parameter	Typical Small Telescopic Mast	High Temperature Application	Design Applicable for Space Station Solar Arrays
Deployed Length	47 ft (14.3 m)	33 ft (10.1 m)	113 ft (34.4 m)
Stowed Diameter	10.0 in (254 mm)	16.0 in (406 mm)	18.5 in (470 mm)
Stowed Length	44.0 in (1,118 mm)	40.4 in (1,026 mm)	83.7 in (2,216 mm)
Total Weight of Mast and Deployer	28.2 lb (12.8 kg)	89 lb (40.4 kg)	217 lb (98.4 kg)
Mast Average Diameter	6.50 in (165 mm)	13.75 in (349 mm)	14.25 in (362 mm)
Stiffness EI, Installed	6.47E+07	3.4E+08	1.17E+09
Bending Strength	3,600 in-lb (n-m)	17,000 in-lb (n-m)	53,000 in-lb (n-m)
Torsion Strength	3,100 in-lb (350 n-m)	25,000 in-lb (2,825 n-m)	57,030 in-lb (6,442 n-m)
Axial Strength	1,400 lb (6,235 n)	4,300 lb (19,151 n)	11,000 lb (48,991 n)
Total Stowed Volume (Diameter)	3,300 in^3 (0.054 m^3)	8,300 in^3 (0.136 m^3)	21,000 in^3 (0.344 m^3)
No. of Telescopic Segments	15	10	18
Material	Graphite/Epoxy Composite	Aluminum and Steel	Graphite/Epoxy Composite

NORTHROP GRUMMAN
Space Technology
Astro Aerospace

Astro Aerospace
Northrop Grumman
Space Technology
6384 Via Real
Carpinteria, CA 93013-1920

www.st.northropgrumman.com/astro-aerospace
e-mail: astro-info@ngc.com

Figure A5-7 Telescopic Mast data sheet, supplied by Northrop Grumman Inc.

A5.5 CoilABLE Masts

The CoilABLE masts supplied by Able Engineering Inc. may be sized by means of these diagrams, sourced from their website at aec-able.com (2006).

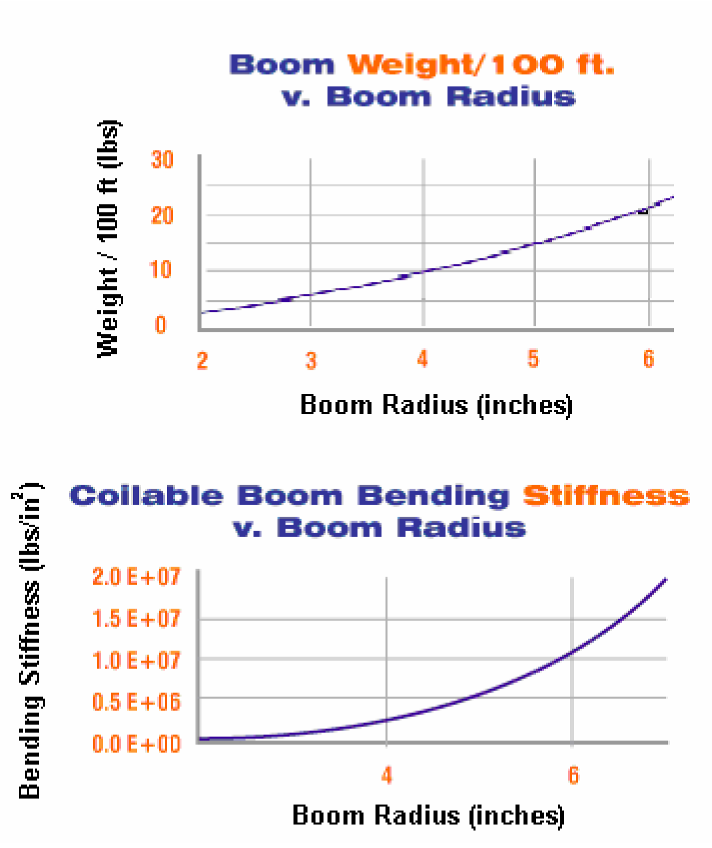

Figure A5-8 CoilABLE mast design diagrams, supplied by Able Engineering Inc.

A5.6 MSP-430

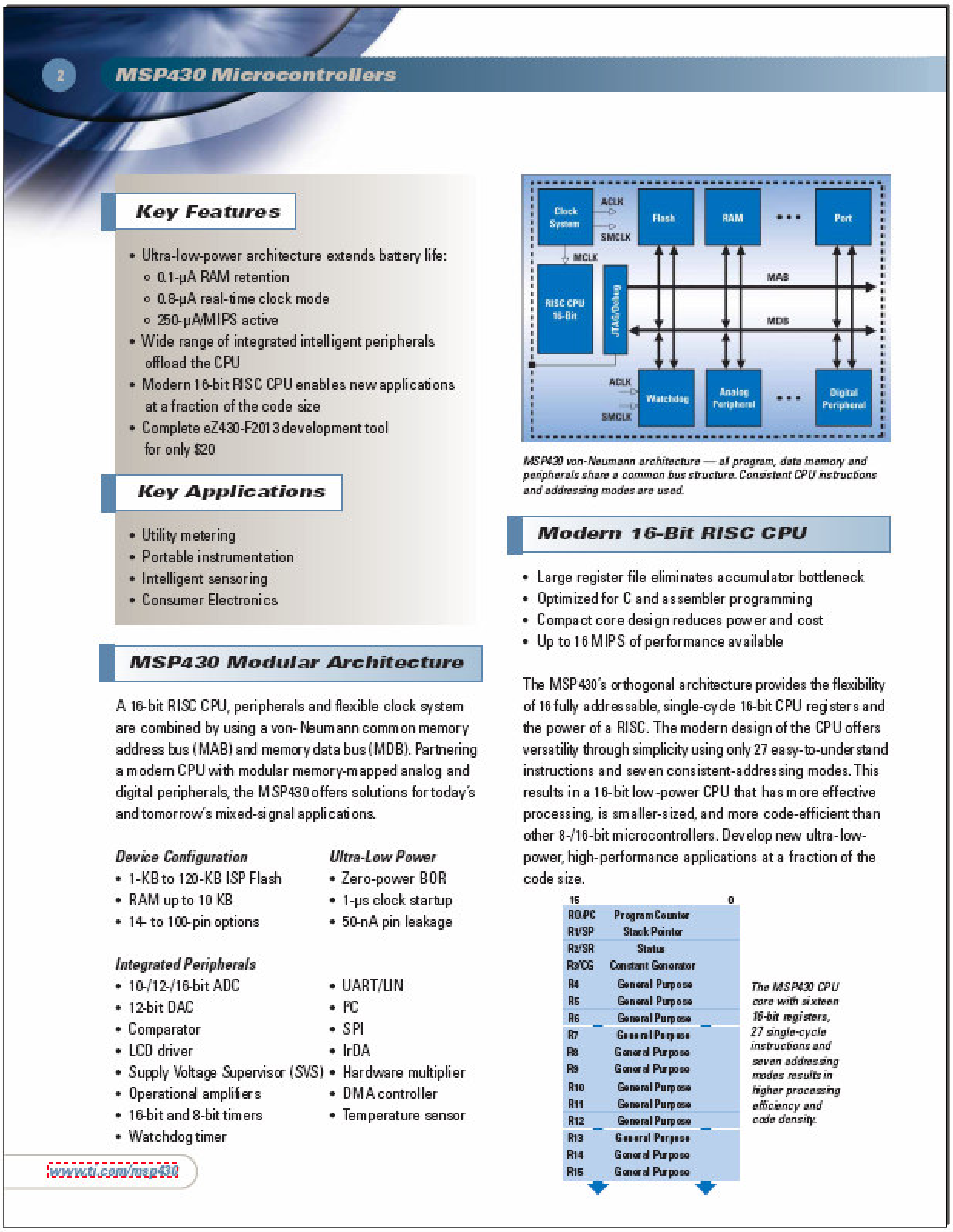

2

MSP430 Microcontrollers

Key Features

- Ultra-low-power architecture extends battery life:
  - 0.1-µA RAM retention
  - 0.8-µA real-time clock mode
  - 250-µA/MIPS active
- Wide range of integrated intelligent peripherals offload the CPU
- Modern 16-bit RISC CPU enables new applications at a fraction of the code size
- Complete eZ430-F2013 development tool for only $20

Key Applications

- Utility metering
- Portable instrumentation
- Intelligent sensoring
- Consumer Electronics

MSP430 Modular Architecture

A 16-bit RISC CPU, peripherals and flexible clock system are combined by using a von-Neumann common memory address bus (MAB) and memory data bus (MDB). Partnering a modern CPU with modular memory-mapped analog and digital peripherals, the MSP430 offers solutions for today's and tomorrow's mixed-signal applications.

Device Configuration
- 1-KB to 120-KB ISP Flash
- RAM up to 10 KB
- 14- to 100-pin options

Ultra-Low Power
- Zero-power BOR
- 1-µs clock startup
- 50-nA pin leakage

Integrated Peripherals
- 10-/12-/16-bit ADC
- 12-bit DAC
- Comparator
- LCD driver
- Supply Voltage Supervisor (SVS)
- Operational amplifiers
- 16-bit and 8-bit timers
- Watchdog timer
- UART/LIN
- I²C
- SPI
- IrDA
- Hardware multiplier
- DMA controller
- Temperature sensor

www.ti.com/msp430

MSP430 von-Neumann architecture — all program, data memory and peripherals share a common bus structure. Consistent CPU instructions and addressing modes are used.

Modern 16-Bit RISC CPU

- Large register file eliminates accumulator bottleneck
- Optimized for C and assembler programming
- Compact core design reduces power and cost
- Up to 16 MIPS of performance available

The MSP430's orthogonal architecture provides the flexibility of 16 fully addressable, single-cycle 16-bit CPU registers and the power of a RISC. The modern design of the CPU offers versatility through simplicity using only 27 easy-to-understand instructions and seven consistent-addressing modes. This results in a 16-bit low-power CPU that has more effective processing, is smaller-sized, and more code-efficient than other 8-/16-bit microcontrollers. Develop new ultra-low-power, high-performance applications at a fraction of the code size.

15	0
R0/PC	Program Counter
R1/SP	Stack Pointer
R2/SR	Status
R3/CG	Constant Generator
R4	General Purpose
R5	General Purpose
R6	General Purpose
R7	General Purpose
R8	General Purpose
R9	General Purpose
R10	General Purpose
R11	General Purpose
R12	General Purpose
R13	General Purpose
R14	General Purpose
R15	General Purpose

The MSP430 CPU core with sixteen 16-bit registers, 27 single-cycle instructions and seven addressing modes results in higher processing efficiency and code density.

Figure A5-9 MSP-430 Controller data sheet, supplied by Texas Instruments Inc.

A5.7 MHX-920

MHX920 OEM Industrial Wireless Modem

The MHX920 is a long range - high speed 900MHz Frequency Hopping Spread Spectrum Modem. The MHX920's rate can be optimized for long distance communication over 60 miles. MHX920 radios offer the fastest communication over the longest distances.

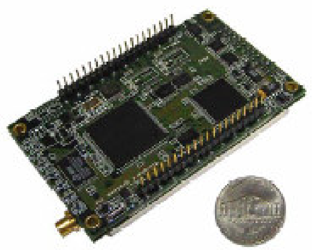

Applications:

- *SCADA (PLCs, Modbus), Telemetry*
- *Security, Surveillance*
- *GPS Vehicle Data/Tracking, DGPS*
- *Electric, Oil, & Gas Utilities/Metering*
- *Display Signs*
- *Traffic Control, Loop detectors*
- *Transparent low latency communication*

If you thought our MHX-910 was good - you'll be amazed with the MHX920. There are many radios that make claims - just run our radios side by side and see what happens.

The MHX920 features robust, high speed, low latency, secure data communications. The MHX920 has a full serial data port and a separate diagnostics port for real-time diagnostics; which does not interfere with data communications. MHX920 offers excellent noise figure, superior interference rejection, very agile frequency synthesis, digital modulation, and matched filter detection. The MHX920 can be user optimized for speed and distance.

Features of the MHX920

- Transparent, low latency link providing true 230 kbps continuous throughput to support protocols such as MODBUS
- Communicates with virtually all PLCs, RTUs, and serial devices
- Industrial Grade - extended temperature specification
- Supports point-to-point, point-to-multipoint, Store and Forward Repeater, TDMA, Multimaster
- Maximum allowable transmit power, (1W)
- Low power consumption in Sleep Mode and High Voltage Option
- 32-bit CRC, selectable forward error correction with retransmit
- Separate diagnostics port - transparent remote diagnosis and online network control
- Backwards and Footprint Compatible with MHX-910

MHX920 HV Option

Rev1.2

MHX920 Specifications (preliminary)

Frequency	902 - 928 MHz
Spreading Method	Frequency Hopping
Band Segments	16 user selectable
Hopping Patterns	128 user selectable
Hopping Channels	minimum 50
Error Detection	32 bit CRC, retransmit on error
Data Encryption	Dynamic Key Substitution
Range	+60 miles (line of sight)
Sensitivity	-108 dBm for BER=1E-6 -110 dBm for BER=1E-4
Output Power	1mW, 100mW to 1W (30dBm)
System Gain	140dB
Data Port Inteface	RS-232/RS485/RS422 TTL or Drivers Level
Serial Baud Rate	300bps to 230.4kbps
Throughput	230.4kbps
Operating Modes	Point-to-Point, Point-to-Multipoint, Store&Forward Repeater, TDMA, Multimaster, Peer to Peer, Transparent
Signals Interface	RxD1, TxD1, RTS, CTS, DCD, DSR, DTR, RxD2, TxD2, RSSI1,RSSI2,RSSI3, Tx LEDs, Rx LEDS, Reset, Config, Wake-up, RSmode, User Analog Input
Diagnostics	Forward & Reflected Power, VSWR, Current, Battery voltage, Temperature, RSSI, Real-time event logging and remote diagnostics
Rejection	Excellent Strong Signal Interference & Rejection Characteristics

Core Voltage	4VDC to 5.5VDC, 7VDC to 30VDC(See option 100)			
IO voltage (user selectable)	3.3VDC to 5.5VDC, RS232/485/422 Levels(See option 100)			
Current (mA)	4 VDC	12 VDC	30 VDC (High Voltage Option)	
Transmit	1200	600	220	
Receive	220	95	40	
Idle	60	20	8	
Sleep	1	1	1	
Antenna Connector	MCX, Reverse SMA (option 110)			
Environment	-40 °C to +75 °C			
Weight	Approx. 80 grams			
Dimensions	Approx. 3.5" x 2.1" x 0.7"			
Approvals	FCC Part 15.247 approved IC RS S210 approved			

Order Options

Option 100	HV OPTION - High Input voltage (7V to 30V) with RS232/RS485/RS422 Drivers
Option 110	Reverse Polarity SMA Connector
Option 200	Class 1 Div 2 (for use in hazardous environments)

Contact Information

AIRLINX Communications, Inc.
Box 253
Greenville, NH 03048
E-mail: sales@airlinx.com
Tel: (888) 224-6814
Fax: (603) 878-0530

Rev1.2

Figure A5-10 Radio Transceiver data sheet, supplied by Microhard Systems Inc.

A5.8 ST 1130 N

BICRON Electronics Company ISO 9001 CERTIFIED

ST1130N

Pull Type Tubular Solenoid
0.43" Dia. × 1.2" L
(11mm × 30.5mm)

Specifications:

- Operation: ....Pull
- Insulation: ....Class "A" (105°C) standard*
- Coil Termination: ....28 AWG flying leads per drawing*
- Plunger linkage: ....Yoke*
- Plunger pole face: ....60° conical*
- Solenoid weight: ....0.59oz [17g]
- Plunger weight: ....0.11oz [3.2g]
- Dielectric Strength: ......1000VAC for one minute
- Operating temperature range: ....-20°C to 40°C

Other options available upon request

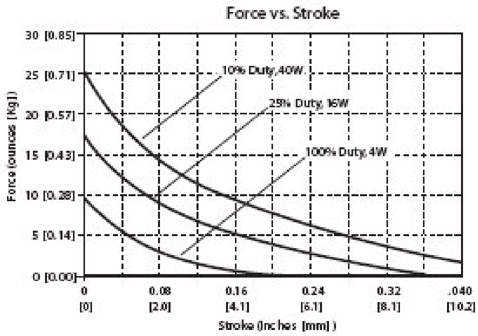

Coil Data:

	100% Duty — 4W		25% Duty — 16W		10% Duty — 40W	
Voltage (VDC)	Resistance (Ω)	Part Number	Resistance (Ω)	Part Number	Resistance (Ω)	Part Number
3	2.3	ST1130N0300	0.56	ST1130N0325	0.23	ST1130N0310
6	9.0	ST1130N0600	2.3	ST1130N0625	0.9	ST1130N0610
12	36.0	ST1130N1200	9.0	ST1130N1225	3.6	ST1130N1210
24	144	ST1130N2400	36.0	ST1130N2425	14.4	ST1130N2410

Typical force @20°C and nominal rated DC voltage. Resistance values ±10% @20°C. All data subject to change. Other voltages and duty cycles available upon request.

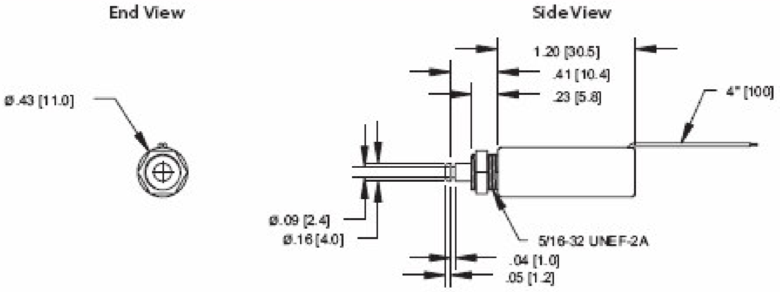

Notes: Solenoid shown in energized position. Dimensions listed are for reference only. Dimensions shown in inches and [mm].

50 Barlow Street • Canaan, CT 06068 • Tel: 860-824-5125 • Fax: 860-824-1137 • www.Solenoid.com • info@Solenoid.com
012002-12658

Figure A5-11 Solenoid data sheet, supplied by the Bicron Electronics Company

Appendix 6 – Effect of Different GSIMs

The deorbit device has been in large part designed with reference to the deorbit times calculated by the Simulink models *Equatorial_Plane.mdl* and *Six_DOF.mdl*. Both of these models made the assumption that any impinging atmospheric particles lose all velocity normal to the drag sail but maintain their full tangential velocity.

This Gas-Surface Interaction Model (GSIM) was chosen because it represents the least possible interaction between the drag sail and the rarefied flow, and thus any conclusions drawn from it regarding the performance of the drag sails will definitely be achieved in reality and may well be exceeded. However, in practice the interaction between the rarefied flow and the drag sail will be greater because there will be some degree of particle reflection, which will have both specular and diffuse elements, as well as tangential velocity losses. The precise degree of interaction depends on a great number of variables such as the gas species, the nature of the surface, the impingement velocity and the temperature. These vary to such an extent that any GSIM which is reasonably accurate for one section of the deorbit may well be unusable elsewhere.

Fortunately this need not affect the design of the deorbit device because it appears that different GSIMs have a scaling rather than differentiating effect of the deorbit times, leaving the optimum design point effectively unchanged. This is illustrated by Figure 8-1, which shows the average deorbit times from 650 km under a GSIM of the opposite extreme - *i.e.* one where the incoming particles are specularly reflected. It can be seen that the optimum apex half-angle remains at approximately 1.4 radians.

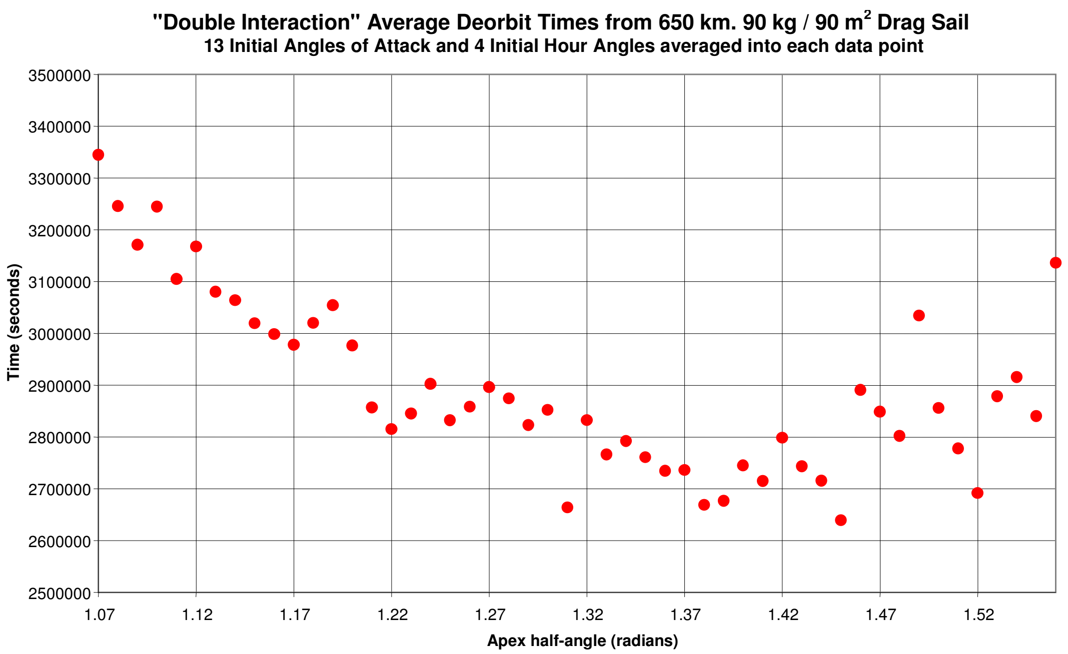

Figure A6-1 Double-interaction Deorbit Times